

ABSTRACT

Title of Thesis: **NON-INVASIVE IMAGING TECHNIQUES
AS A QUANTITATIVE ANALYSIS OF
SKIN DAMAGE DUE TO IONIZING
RADIATION**

Abby Jeanne Vogel, Master of Science, 2004

Thesis Directed By: **Yang Tao, Ph.D., P.E., Professor of Biological
Resources Engineering**

This study tested the ability of two non-invasive techniques, thermography and near-infrared multi-spectral imaging, to quantitatively assess the response of mouse skin to a single dose of X-ray irradiation. Thermal images from an 8-12 micron thermal camera were recorded after a cold stimulation to see the thermal recovery of the skin. The irradiated areas showed a significantly faster thermal recovery than the non-irradiated areas two weeks after radiation ($p < 0.05$).

The NIR multi-spectral imager obtained images at six specially selected wavelengths between 700 and 1000 nm. Two-layer model-based diffuse reflectance spectroscopy monitored changes in blood oxygen saturation and blood volume. Blood oxygen fractions were significantly lower after radiation ($p < 0.05$). Blood volume changed in six of seven irradiated mice one week after radiation. The non-invasive imaging techniques were successful in quantitatively analyzing the response of the skin to a single dose of irradiation.

NON-INVASIVE IMAGING TECHNIQUES AS A QUANTITATIVE ANALYSIS
OF SKIN DAMAGE DUE TO IONIZING RADIATION

By

Abby Jeanne Vogel

Thesis submitted to the Faculty of the Graduate School of the
University of Maryland, College Park, in partial fulfillment
of the requirements for the degree of
Master of Science
2004

Advisory Committee:

Professor Yang Tao, Chair

Professor and Chair Fredrick Wheaton

Professor and Associate Chair Nam Sun Wang

Dr. Amir Gandjbakhche, National Institutes of Health

© Copyright by
Abby Jeanne Vogel
2004

Acknowledgements

I would first like to thank my thesis advisor at the University of Maryland, Dr. Yang Tao, for his invaluable guidance and motivation throughout all aspects of this research. I would also like to thank my research supervisor, Dr. Amir Gandjbakhche, of the National Institutes of Health, Laboratory of Integrative and Medical Biophysics, Section on Biomedical Stochastic Physics, for his helpful advice and ability to provide me with the funding and resources necessary to complete this thesis research.

I would also like to thank my other committee members, Dr. Fredrick Wheaton and Dr. Nam Sun Wang, for their time, support, and helpful criticism.

Additionally, I would like to express my appreciation to all members of the Section on Biomedical Stochastic Physics at the National Institutes of Health. I especially thank Dr. Moinuddin Hassan and Dr. David Hattery for all their help with the experiments and analyses necessary to complete this thesis. I would also like to thank Dr. Angelo Russo and Ms. Anastasia Sowers of the Radiation Biology Branch at the National Institutes of Health who provided invaluable mice and expertise.

Finally, I would like to extend my deepest gratitude to my family and friends for their love and support during the past two years.

Table of Contents

Acknowledgements.....	ii
Table of Contents.....	iii
List of Tables.....	v
List of Figures.....	vi
Chapter 1: Introduction.....	1
Chapter 2: Literature Review.....	3
2.1 Skin.....	3
2.1.1 Epidermis.....	4
2.1.2 Dermis.....	5
2.2 Ionizing Radiation.....	7
2.2.1 Radiation Dose.....	7
2.2.2 Radiation Tolerance.....	8
2.3 Ionizing Radiation Effects.....	9
2.3.1 Early Erythematous Reaction.....	10
2.3.2 Main Erythematous Reaction.....	10
2.3.3 Late Phase Reactions.....	11
2.3.4 Late Skin Damage.....	13
2.4 Fibrosis.....	13
2.5 Analyzing Radiation-Induced Changes.....	14
2.5.1 Vascular Changes.....	14
2.5.2 Collagen Changes.....	17
2.5.3 Skin Layer Changes.....	21
2.6 Grading Fibrosis Reaction.....	23
2.6.1 Qualitative Methods.....	23
2.6.2 Quantitative Methods.....	26
2.7 Thermography.....	28
2.7.1 Infrared Light.....	28
2.7.2 Thermography Camera.....	29
2.7.3 Static Thermography.....	30
2.7.4 Time-Response Thermography.....	31
2.8 Laser Doppler Imaging.....	33
2.8.1 Laser Doppler Imaging Technique.....	33
2.8.2 Laser Doppler Imaging Applications.....	34
2.9 Near-Infrared Multi-Spectral Imaging.....	35
2.9.1 Near-Infrared Multi-Spectral Imaging Technique.....	35
2.9.2 Near-Infrared Multi-Spectral Imaging Applications.....	36
Chapter 3: Objectives.....	38
Chapter 4: Materials and Methods.....	39
4.1 Mice.....	39
4.1.1 Mouse Selection and Care.....	39
4.1.2 X-ray Irradiation Procedures.....	40
4.1.3 Plexiglass Holder.....	41

4.2 Imaging Procedures	42
4.3 Thermography.....	43
4.3.1 Thermal Camera.....	43
4.3.2 Thermography Procedure.....	44
4.3.3 Preliminary Analyses.....	45
4.3.4 Final Selected Analysis.....	47
4.4 Laser Doppler Imaging	48
4.4.1 Laser Doppler Imager	48
4.4.2 Laser Doppler Imaging Procedures	49
4.4.3 Laser Doppler Imaging Analysis	49
4.5 Near-Infrared Multi-Spectral Imaging.....	50
4.5.1 Near-Infrared Multi-Spectral Imager.....	50
4.5.2 Near-Infrared Multi-Spectral Imaging Analysis.....	51
Chapter 5: Results and Discussion.....	55
5.1 Thermography.....	55
5.1.1 Changes in Thermal Recovery Times.....	55
5.1.2 Discussion of Changes in Thermal Recovery Times.....	58
5.2 Laser Doppler Imaging	60
5.2.1 Changes in Blood Flow.....	60
5.3 Near-Infrared Multi-Spectral Imaging.....	61
5.3.1 Changes in Blood Oxygen Fraction.....	61
5.3.2 Changes in Blood Volume.....	66
5.3.3 Discussion of Changes in Blood Oxygen Fraction and Blood Volume.....	68
Chapter 6: Conclusions.....	72
Chapter 7: Suggestions for Further Study.....	73
Appendix A.....	75
A.1 Thermal Recovery Results.....	75
A.2 Laser Doppler Imaging Results.....	76
A.3 Near-Infrared Multi-Spectral Imaging Results	77
Bibliography	80

List of Tables

Table 1. Mouse leg skin reaction (Iwakawa, 2003).	24
Table 2. Date of significant decrease in blood oxygen fraction and the factor by which the fraction decreased for each radiated mouse.	65
Table 3. Temperature difference of the left non-irradiated area in °C from the center irradiated area.	75
Table 4. Temperature difference of the right non-irradiated area in °C from the center irradiated area.	76
Table 5. Laser Doppler imaging blood flux of mice on day 0.	76
Table 6. Oxygen blood fraction analysis of radiated and control mice.	77
Table 7. Blood volume analysis of radiated and control mice.	79

List of Figures

Figure 1.	Structure of the epidermis, dermis and subcutaneous layers of the skin (http://skincancer.dermis.net/content/e01geninfo/e7/index_eng.html).	4
Figure 2.	Photomicrograph illustrating late skin reactions. The red arrows point to the distorted collagenous bundles seen in the dermis layer of the skin and the green arrows show the thin epidermis layer (Archambeau, 1985).	12
Figure 3.	Photomicrograph illustrating late skin reactions. The deeper vessels, outlined in red, increased significantly in diameter after irradiation (Archambeau, 1985).	16
Figure 4.	Structural formation of collagen (Griffiths, 2000).	18
Figure 5.	Immunohistochemical staining of human breast skin. The arrows represent the number of PINP-positive fibroblasts (a) before irradiation and (b) after irradiation (Autio, 1998).	20
Figure 6.	Thermogram of left shoulder and back of patient with a vascular tumor (Kaposi's Sarcoma Protocol, NCI, NIH).	30
Figure 7.	Static thermographic image and Tau image of Raynaud's phenomenon secondary to scleroderma (Merla, 2002). The colorbar shows the recovery time in minutes of each image pixel. The areas associated with longer recovery times (blue) identify with the main damaged areas.	33
Figure 8.	Laser Doppler imaging technique.	34
Figure 9.	Laser Doppler image shows blood flow through veins (Kaposi's Sarcoma Protocol, NCI, NIH).	35
Figure 10.	Schematic of the near-infrared multi-spectral imaging system. The Filter wheel in front of the CCD camera contains six filters of 700, 750, 800, 850, 900, and 1000 nm.	36
Figure 11.	700 nm spectral and oxy-hemoglobin fraction images. The top image shows a lesion area and the bottom image shows a contralateral lesion-free area (Kaposi's Sarcoma Protocol, NCI, NIH).	37
Figure 12.	NCr athymic nude immunocompromised female mouse.	39
Figure 13.	Plexiglass holder designed and manufactured to decrease movement of mice during imaging.	42
Figure 14.	Plexiglass holder with mouse legs and tail taped down for limited movement.	42
Figure 15.	Block diagram of three imaging techniques (near-infrared multi-spectral imaging, thermography, and laser Doppler imaging) and images collected during each experiment.	43
Figure 16.	Thermovision Alert 8-12 micron thermal camera (SC500) (FLIR, 2002).	44
Figure 17.	Static thermal image shows the temperature heterogeneity of a control mouse. The control mouse varies in temperature from 30-34 °C. The area on the left of the control mouse, closer to the leg, was generally cooler than the center area, which was cooler than the area on the right, closer to the head.	45

Figure 18. Digital image of mouse shows the three ROIs selected for thermal imaging analysis: (1) Left, non-irradiated area; (2) Center, irradiated area; and (3) Right, non-irradiated area.	48
Figure 19. Laser Doppler imager (moorLDI-2λ) (Moor-LDI, 2002).	49
Figure 20. Near-infrared multi-spectral imager.	50
Figure 21. 850 nm near-infrared multi-spectral image of mouse.	51
Figure 22. Absorption coefficient spectra for oxy-hemoglobin, deoxy-hemoglobin, and water.	52
Figure 23. Typical result of reheating temperature differences of the left and right non-irradiated areas from radiated area of Frame 100 after the cold stimulation minus the initial temperature of the mouse on day 0 and week 2. Control mice are c_1 and con_3 and radiated mice are 32_1 and 32_2.	56
Figure 24. Differences in temperatures of irradiated (center) and non-irradiated (left and right) areas from the pre-stimulation temperature for (a) Control (#2) mouse at two weeks; and (b) 32 Gy (#2) mouse two weeks after radiation.	57
Figure 25. Difference in temperature of Frame 100 after the cold stimulation minus the pre-stimulation average temperature for the 32 Gy (#2) radiated mouse two weeks after radiation.	58
Figure 26. 32 Gy mouse (#2) two weeks after radiation in (a) Digital image with aluminum foil pieces covering the India ink tattoos. Red area inside tattoos is irradiated area showing desquamation; and (b) Static thermal image before cold stimulation showing affected areas to be colder in the image.	59
Figure 27. Blood flux of 32 Gy (#1) mouse (top) before cold stimulation and (bottom) after cold stimulation. The differences in blood flux were found to be not significant before and after the cold stimulation ($p < 0.05$) for all mice.	60
Figure 28. Laser Doppler blood flux values on day 0 before and immediately after the cold stimulation. No significant differences were found in the blood flow before and after the cold stimulation among all of the mice ($p < 0.05$).	61
Figure 29. Oxygen blood saturation images of 32 Gy (#2) mouse (a) at day 0 before radiation; and (b) two weeks after radiation was applied. High oxygen saturation inside the radiated area before radiation was no longer present two weeks after radiation.	62
Figure 30. Oxygen blood saturation of 30 Gy (#1) mouse (a) at day 0 before radiation; and (b) two weeks after radiation was applied. High oxygen saturation inside the radiated area before radiation was no longer present two weeks after radiation.	63
Figure 31. Blood oxygen fractions of control mice on day 0 and week 1. No significant differences were seen in blood oxygen fractions of the control mice ($p < 0.05$).	65

Figure 32. Blood oxygen fractions before and after radiation. Values after radiation were selected at the date of initial significant decrease in blood oxygen fraction from Table 2.	66
Figure 33. Blood volume of 32 Gy (#1) mouse (a) before radiation at day 0; and (b) one week after radiation was applied. Inside the tattooed area, day 0 shows very small blood volume (mean = 0.09). One week after radiation, the tattooed area appears to have much higher blood volume (mean = 0.26).	67
Figure 34. Blood volume of 35 Gy (#1) mouse (a) before radiation at day 0; (b) one week after radiation was applied; and (c) two weeks after radiation was applied.	67
Figure 35. Blood volume of 30 Gy (#3) mouse (a) before radiation at day 0; and (b) one week after radiation was applied.	68
Figure 36. (a) Digital image of control mouse showing wrinkles; and (b) Reconstructed blood oxygen saturation of same control mouse showing non-homogeneity of saturation where wrinkles are present.	69
Figure 37. (a) Digital image of mouse showing spread of fingernail polish issue around aluminum foil pieces; and (b) Blood oxygen saturation showing fingernail polish areas. Areas with visible fingernail polish appeared to have lower blood oxygen saturation than the rest of the irradiated area.	70
Figure 38. Blood oxygen fraction of the 32 Gy mouse (#1) two weeks after Radiation showing bilateral pattern of oxygen re-saturation.	70

Chapter 1: Introduction

The response of the skin to ionizing radiation has important implications for both the treatment of malignant disease by radiation and for radiological protection. After undergoing radiation therapy as cancer treatment, a patient's skin responds in many ways; one of the most debilitating is the formation of fibrosis, or thick rough skin. Radiation damage, including fibrosis, can be permanent, but its onset and chronic extension have been poorly understood. The objective of this research was to develop a means of optically and non-invasively quantifying radiation damage in mouse skin. Some of the effects of radiation have been documented in pathological, biochemical, and cell culture studies. These experiments have shown radiation-induced changes in collagen production, vascularization, protein levels, and the structure and cell populations of the epidermis and dermis layers of the skin.

By invasive techniques and visual assessments, the progression of damage after ionizing radiation has been highly reproduced for both mice and pigs receiving a single dose of irradiation. The goal of this collaboration at the National Institutes of Health between the National Institute of Child Health and Human Development (Laboratory of Integrative and Medical Biophysics, Section on Biomedical Stochastic Physics) and the National Cancer Institute (Radiation Biology Branch) was to quantitatively assess the onset and extent of radiation damage using non-invasive optical imaging techniques. The non-invasive techniques were thermography and near-infrared multi-spectral imaging. A sequence of thermal images from an 8-12 micron wavelength thermal camera (FLIR, 2002) were recorded after a one minute, thirty second cold stimulation to determine

differences in the reheating response of the irradiated and non-irradiated skin. The near infrared multi-spectral imaging system contained a high-resolution CCD portable camera (Princeton Instruments, Trenton, NJ). A white light held approximately 50 cm from the mouse skin illuminated the area uniformly. Using optical filters, images were obtained at six specially selected wavelengths between 700 and 1000 nm. Two-layer model-based diffuse reflectance spectroscopy monitored changes in blood volume and blood oxygen fraction. These experimental and analysis methods could allow the monitoring of human subjects being treated with anti-fibrotic agents to lessen their normal tissue reaction to radiation.

Chapter 2: Literature Review

2.1 Skin

In order to understand the effects of radiation on the skin, one must first understand the characteristics and structure of the skin. Skin is the flexible tissue enclosing the body of vertebrate animals while providing vital protective and metabolic functions. The skin provides a barrier against invasion by outside organisms, protects underlying tissues and organs from abrasion and other injury, and shields the body from the dangerous ultraviolet rays in sunlight. It also waterproofs the body, preventing excessive loss or gain of bodily moisture.

At the human/environment interface, heat is carried away from the body by conduction, convection, radiation, and evaporation. The human thermoregulatory system maintains a reasonably constant body temperature against a wide range of environmental conditions. This is enabled due to the body's numerous sweat glands excreting waste products along with salty moisture; its fat cells acting as insulation against cold; and when the body overheats, its extensive small blood vessels carrying warm blood near the surface to be cooled. The skin is lubricated by its own oil glands, which keep both the outside layer of the epidermis and the hair from drying to brittleness. The body uses several physiological processes to increase or decrease heat transfer with the environment. The mechanism controlling thermal emission and dermal microcirculation is driven by the sympathetic nervous system. In the presence of a disease affecting the

local thermoregulatory system there may be an altered sympathetic function and a change in the local metabolic rate (Merla, 2002).

Skin, shown in Figure 1, contains two main layers of cells: a thin outer layer, the epidermis; and a thicker inner layer, the dermis, which is bonded to a subcutaneous fat layer which may be several centimeters thick (Archambeau, 1995).

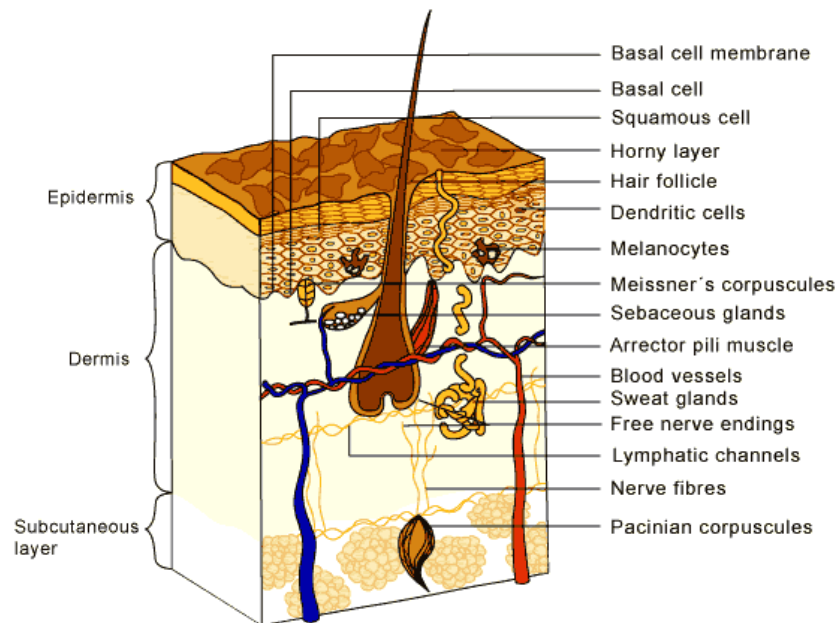


Figure 1. Structure of the epidermis, dermis and subcutaneous layers of the skin (http://skincancer.dermis.net/content/e01geninfo/e7/index_eng.html).

2.1.1 Epidermis

The epidermis is seen in Figure 1 on the surface of the skin and is usually between 30 to 300 μm thick (Archambeau, 1995). The epidermis has no blood vessels, but does contain keratinocytes, melanocytes, dendritic cells, and basal cells. Along the internal surface of the epidermis, keratinocytes are stacked on top of each other, forming sub-

layers. The keratinocytes develop at the bottom and rise to the top, where they flatten and overlap to form a tough membrane, and gradually shed as calluses or collections of dead skin. Basal cells are found at the bottom of the epidermis.

Cell proliferation occurs in the basal cell monolayer with a generation time of 2.6 days. About four percent of the cells move into and out of the layer daily, maintaining constant population densities (Archambeau, 1995). Melanocytes, located in the lower basal cell layer of the epidermis, produce a dark pigment called melanin which contributes to skin color and provides ultraviolet protection. Dendritic (Langerhans) cells are involved in the epidermal immune system. They engulf foreign material that invades the epidermis and migrate out of the skin to stimulate an immune response. The five layers of the epidermis that work together to continually rebuild the surface of the skin from within while maintaining the skin's epidermal strength include the basal cell layer, the squamous cell layer, the stratum granulosum, the stratum lucidum, and the stratum corneum.

2.1.2 Dermis

The underlying dermis, much thicker than the epidermis, consists of connective tissues that contain embedded blood vessels, nerve endings, muscles, hair follicles, sweat glands, sebaceous glands, fat cells, and collagen (Figure 1). The dermis is 1-3 mm thick. The upper 350 μm portion is the papillary layer, which contains the microvessels supplying the epidermis. Nerve endings respond to various stimuli, including contact, heat, and cold. Meissner's corpuscle is effective in detecting light touch and soft, fleeting movements. Pacinian corpuscles function as receptors for deep pressure and vibration.

Response to cold activates the erector muscles, causing hair or fur to stand erect. From the outer surface of the dermis extend numerous projections (papillae) that fit into pits on the inner surface of the epidermis so that the two layers are firmly locked together.

The vascular supply to the dermis is largely from segmental arteries, each of which supplies a relatively small area of the epidermis with nutrients. The dermal vasculature includes arteries and veins from the subcutaneous layer that pass through the dermis with minimal branching. Tufts containing arterioles, venules, and capillaries extend through the papillary dermis up to the epidermal basal lamina. These vessels are contained in a loose connective tissue (Archambeau, 1985). They exist as separate folded and coiled geographically isolated tufts, or bunches, with no interconnection to adjacent tufts except by arteries and veins (Archambeau, 1995). Since the human skin has a rich blood supply, it has remarkable self-healing properties, particularly when only the epidermis is damaged. Deeper wounds, penetrating to the underlying tissue, heal by scar formation.

Sebaceous (oil) glands are small, sacculated organs that secrete sebum. This oily substance is a natural moisturizer which conditions the hair and skin. Sebaceous glands are found all over the body, but they are more numerous in the scalp area and around the forehead, chin, cheeks, and nose.

The dermis tissues are composed largely of collagen fibers, approximately 75% by dry weight (Hopewell, 1990). Collagen is responsible for the skin's pliability and mechanical resistance and is also involved in the regulation of the body temperature (see 2.5.2 for further collagen information). This research suggests that skin structures and properties described above change as a result of ionizing radiation.

2.2 Ionizing Radiation

Ionizing radiation is radiation that has enough energy to remove electrons from atoms or molecules when it passes through or collides with a material. The loss of an electron with a negative charge that causes an atom to become positively charged is called ionization. When ionizing radiation interacts with skin, it gives its energy to the body tissues (NIH, 2002).

X-rays and γ -rays are the most popular types of ionizing radiation. X-ray irradiation is generated when a strong electron beam bombards metal inside a glass tube. The frequency of this radiation is very high: $0.3\text{-}30 \times 10^{18}$ Hertz (Canada, 2002). Gamma rays are massless, chargeless waves of energy emitted from the nuclei of metals undergoing a decaying process and penetrate substances such as paper, skin, and wood. Gamma irradiation causes severe damage to skin and internal organs (USA, 2002). The main difference between these two types of ionizing radiation is that X-rays originate in the electromagnetic field surrounding the nucleus whereas γ -rays are created in the nucleus. The amount of ionizing radiation a patient receives is referred to as the radiation dose.

2.2.1 Radiation Dose

Absorbed radiation dose, or the amount of energy absorbed per unit weight of the organ or tissue, is expressed in units of gray (Gy) or rad. One Gy dose is equivalent to one joule of radiation energy absorbed per kilogram of tissue weight. Rad is the older but still used unit of absorbed dose. The conversion factor from Gy to rad is that one gray is equivalent to 100 rad (FDA, 2003). To better understand relative dose levels, doses of

30, 32, and 35 Gy were applied in this research. A typical dose for an adult mandibular molar radiograph taken at the dentist office is 4 mGy and 65 mGy for a standard adult panoramic radiograph (Napier, 1999). The doses of radiation in this experiment were for cancer treatment and were much larger than a normal X-ray in a doctor's office.

The effective dose is regarded as an expression of dose in terms of its biological effect. Data recorded from conventional X-ray examinations and compiled by the National Radiological Protection Board (NRPB) regarding typical effective doses of diagnostic radiographic procedures of patients in 380 hospitals throughout the United Kingdom from 1990 to 1995. Typical effective doses for common diagnostic radiologic procedures ranged from the equivalent of a day or two of natural background radiation (for a chest radiograph) to 4.5 years (for computed tomography of the abdomen) (NRPB, 2000). However, there is substantial variation in the background radiation between and within countries.

2.2.2 Radiation Tolerance

Tissue has a normal radiation tolerance. In the skin, the rapidly dividing cells (keratinocytes, hair follicles, and sebaceous glands) are more sensitive to radiation while the cells of the sweat glands and connective tissue are more resistant. For cancer patients, the total dose of radiation is divided to allow some recovery of the skin between treatments. The skin tolerance decreases as the area irradiated increases. The radiosensitivity of any tissue is directly proportional to the cell-renewal requirements of that tissue and the stage of the cell cycle.

The dose limit of the skin to radiation depends on many factors. For high dose

irradiations, dermal atrophy and possible telangiectasia are cosmetically unacceptable late changes that could determine the dose limit. The threshold dose seen in human skin for the onset of telangiectasia has been shown to be about 65 Gy when given in fractions, with a threshold dose of about 40 Gy (Hopewell, 1990). Tissue oxygenation does not decrease with time after radiation therapy and impaired blood supply in irradiated skin is unlikely to be the sole cause of impaired healing (Lopez, 1998). Radiation therapy can cause low levels of white blood cells and platelets (NIH, 2003).

Effective radiation therapy for the treatment of tumors eventually causes degenerative changes in the surviving tissue, which can result in complications. Though the techniques and technologies for radiotherapy have been improved, skin reactions and complications still occur and continue to be a problem.

2.3 Ionizing Radiation Effects

Methods that study the degeneration of tissue as a result of irradiation are invasive. Different types of ionizing radiation (X-ray and γ -ray) and subjects (humans, mice, and pigs) have tested the effects of radiation on the skin. There are seven major factors that determine the effects of ionizing radiation: site of radiation, radiation field, time-dose fractionation, volume of tissue irradiated, radiosensitivity of the tissue, oxygen availability, and nutritional status of the patient. Skin effects associated with radiation therapy occur from days to months after therapy, depending on the survival and integrity of the proliferative basal cells of the epidermis and connective tissue. A timeline of visible effects has been created for all doses in the range of 20-60 Gy, showing dose independency (Russo, 2002). The skin effects begin immediately, within 24 hours after

irradiation, with a mild blush of erythema (redness) in the irradiated skin, which rapidly resolves by 48 hours. This is described below as the early erythematous reaction. Thereafter, there are no additional observable changes in the skin until 16 days post irradiation, whereupon the skin becomes erythematous. On day 17-18, the mice lose hair in the irradiated area and by day 21, the skin begins to desquamate (shed). Dry desquamation rapidly progresses to wet desquamation by day 26. After day 26, the skin completely heals over and only course, rough alopecic skin is noted in the irradiated area. This sequence of events is detailed below as the main erythematous reaction. The borders of the irradiated skin are crisply demarcated. With time, the irradiated skin develops increasing fibrosis, a late phase reaction. Within one year, the animals start to show signs of arteriovenous shunting and telangiectasia, clear characteristics of late skin damage. Radiation has been shown to cause an early erythematous reaction, a main erythematous reaction, a late phase reaction, and late skin damage, effects of which can last for years.

2.3.1 Early Erythematous Reaction

The early erythematous reaction seen within one day after radiation is thought to be related to inflammation. As a result of the activation of proteolytic enzymes, the permeability of the capillaries has been shown to increase (Hopewell, 1990). These acute changes can be painful and debilitating (Archambeau, 1995).

2.3.2 Main Erythematous Reaction

The main erythematous manifestations occur within weeks after irradiation and includes erythema, vesiculation, dry desquamation, moist shedding of the skin, and hair

loss. The clinically irradiated skin appears dry because of sweat and sebaceous gland destruction. During this reaction, the basal cell population of the epidermis is targeted and a second reddening of the skin occurs. The radiation causes a linear loss of cells from the basal layer, which reaches a peak at 17-21 days, and accounts for the first appearance of moist desquamation (Archambeau, 1995). The rate of cell loss in mice is 8.3 percent per day, which is faster than the rate in humans. The thickening of the outer layer of the epidermis (stratum corneum), known as dry desquamation, peaks during 17-21 days (Hopewell, 1990).

The exponential re-population of the basal layer of the epidermis after radiation is due to the proliferation of the cells from within the irradiated area. After an area of irradiated skin is completely stripped of epithelial cells, then the healing by moist desquamation occurs as a result of the division and migration of viable cells from the edges of the irradiated area (Hopewell, 1990). This re-epithelialization shows basal cells return to control levels and above by 28-32 days. Complete regeneration of the epidermis is produced at all doses up to 45 Gy (Archambeau, 1995). This healing is represented by the progressive loss of crust, which is usually complete by 36 days. However, higher doses develop a second reaction of necrosis or ulceration between 36-70 days (Archambeau, 1985). After the main erythematous reaction, late phase reactions, including fibrosis, are seen in the skin. The severity of the early skin effects does not necessarily predict the severity of late changes.

2.3.3 Late Phase Reactions

The late phase reactions of radiation therapy occur slowly, for months after

irradiation and vary in their severity. At the maximum, the skin is characterized by a dusky or mauve appearance. In pigs, the late phase of erythema and dermal necrosis develops after a latency of 70-120 days. Necrosis is shown to be preceded by a loss of endothelial cells, a reduction in capillary density, and a dose-related decline in dermal blood flow.

Fibrosis occurs as a late phase reaction, more than ten weeks following radiation and is characterized by a progressive hardening, swelling, and thickening of the dermis and subcutaneous tissues. It is most severe in those areas where there is an earlier moist reaction. Fibrosis onset is dose-dependent and progression is slowly progressive (see 2.4 for more detailed information). After fibrosis is present, the papillary dermis consists of a layer of multiple distorted acellular collagenous bundles. In obese areas there is extensive cellular fibrosis that lacks a consistent pattern (Archambeau, 1995). Figure 2 shows the late phase reactions with a thin atrophic epidermis and a smooth, but scaling, outer surface.

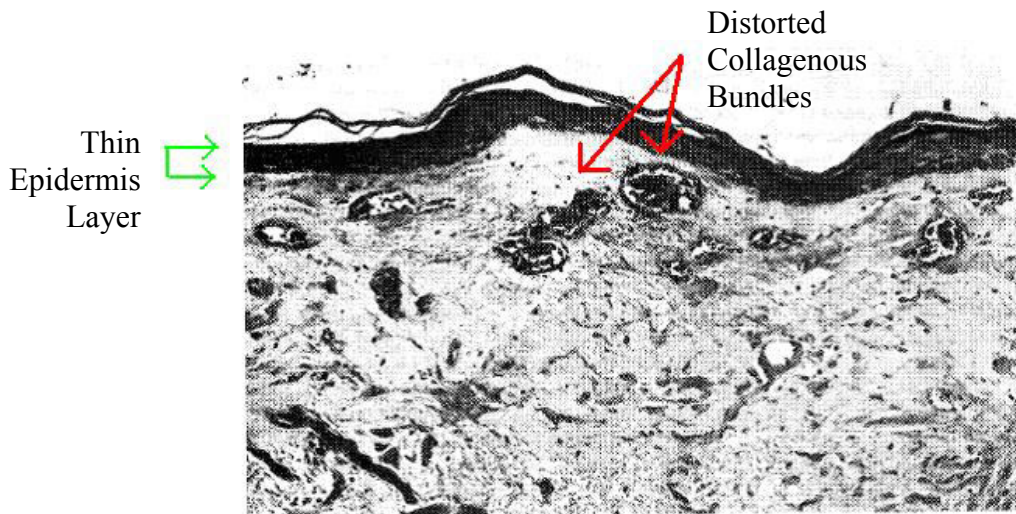


Figure 2. Photomicrograph illustrating late skin reactions. The red arrows point to the distorted collagenous bundles seen in the dermis layer of the skin and the green arrows show the thin epidermis layer (Archambeau, 1985).

The dermis is markedly hypocellular and consists of dense degenerative collagen and elastic tissues and fibrosis. The red arrows point to the distorted collagenous bundles in the dermis. The green arrows show the very thin epidermis layer. After the late phase reactions, late skin damage appears at least one year after radiation.

2.3.4 Late Skin Damage

Late skin damage is determined by a change in the configuration of blood vessels, known as telangiectasia. This reaction develops in the atrophic dermis under a thinned epidermis as an area of reddish discoloration. The reaction exhibits multiple, prominent, thin-walled, and dilated vessels. Telangiectasia is rarely seen earlier than 52 weeks after radiation, but increases in incidence and severity for up to at least ten years. In humans, a five percent incidence of telangiectasia has been reported after five years with a radiation dose of 45 Gy (Archambeau, 1995). The incidence is thought to be dose dependent. Skin reactions after ionizing radiation exposure have been shown to last for years, even lifetimes.

2.4 Fibrosis

One of the major chronic side effects of radiation therapy in many tissues is fibrosis. Fibrosis can be found in many tissues including the skin, heart, liver, kidney, submucosa of gastrointestinal and urinary tracts, and the lung. Depending on the area involved, fibrosis can lead to ulceration with poor wound healing, impaired range of motion, swallowing problems, and neuropathy in humans. Fibrosis is the formation of new tissue, a scar, in the irradiated area, and is characterized by the excessive shortening of muscles; an abnormal number of normal cells; a decrease in vascular blood supply;

and excessive amounts of collagen, fibronectin, and other extracellular matrix proteins. The overproduction and deposition of large amounts of collagen cause the skin to become thickened and inflexible.

Growth factors are thought to play a pathogenic role in fibrosis formation. It is believed that fibrotic tissue remodeling results from the overproduction of fibrogenic cytokines which modulate the growth and secretion of fibroblasts, including insulin-like growth factor (IGF-1), transforming growth factor (TGF- β 1), and platelet-derived growth factor (PDGF) (Burger, 1998). These biochemical events are accompanied by pronounced cellular changes in the fibroblast cell system. Alterations of fibroblast proliferation and the appearance of radiation fibroblasts have long been thought to be the cellular cause of radiation-induced fibrosis in many tissues. Studies have suggested that in fibroblasts, the expressions of the cell phenotypes *in vivo* and *in vitro* are greatly altered and that growth factors play important roles in promoting and regulating the late fibrotic process (Lefaix, 1999). Changes in the skin after radiation have been correlated to the onset and extent of fibrosis.

2.5 Analyzing Radiation-Induced Changes

Besides the visible effects of radiation on the skin, vascular, structural, and chemical changes in the skin have also been detected. Scientists have tested many invasive and non-invasive methods to quantitatively assess the radiation-induced changes in the skin's vascularity, epidermis and dermis layers, and collagen content.

2.5.1 Vascular Changes

The injurious effect of irradiation on the vascular system has not been studied

extensively by non-invasive techniques. In an invasive approach, Archambeau (1985) performed experiments on swine skin with single doses of radiation between 16-26 Gy. The irradiated area was biopsied and the animals were killed for 1-70 days following irradiation. A vascular model was created for the 70 day period. The study showed that there were no morphologic changes in the microvasculature until the epidermal remnant was lost, around 25 days. At that time, an inflammatory infiltrate and focal edema occurred in the upper dermis beneath the eroded area. After 28 days, vascular dilatation began. The endothelial vessel loss continued with higher doses until the epidermis was lost. Then, the vascular lumen diameters increased reaching a maximum of seven times the control and vessels containing microthrombi were present. From 32-49 days after irradiation, Archambeau showed an uncoiling of vessels, with shortening and dilatation, which formed a single vertical tube. The principal morphologic consequence was the fragmentation and alteration of the vascular islands. There was cell loss followed by a decrease in the number of lumen cross sections and a change in the connective tissue around the vascular islands. The islands appeared fragmented with a loss of detail and increased disorganization. By days 43-49, the vascular units appeared as isolated, dilated single vessels set in an edematous matrix. The few remaining vessel lumens appeared more elongated than circular (Archambeau, 1985). Figure 3 illustrates the changes in the deeper vessels. The deeper vessels, outlined in red, attained such a large size that they were readily discernable from the skin surface.

In a related study, preliminary data showed that irradiated vessels following 16.5 and 23.4 Gy doses of irradiation increased in average diameter over non-irradiated vessels by a factor of two after 57 and 43 days, respectively. The vessels with diameters

less than ten micrometers decreased in diameter by about 50% (Archambeau, 1995). Other scientists have used histologic examination to observe dilated blood vessels (Gottlober, 2000).

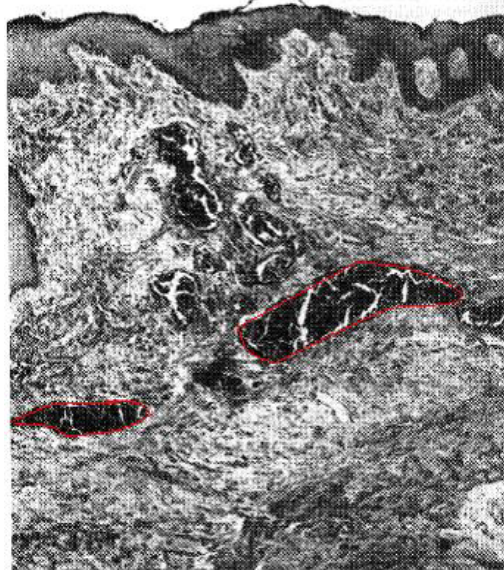


Figure 3. Photomicrograph illustrating late skin reactions. The deeper vessels, outlined in red, increased significantly in diameter after irradiation (Archambeau, 1985).

In 1975, De Ruiter was interested in determining if blood flow changed after radiation. He performed an experiment with X-ray irradiation to investigate the blood flow and permeability in subcutaneous tissue. An X-ray dose of 30 Gy was applied to the tails of mice by means of the local clearance method. The mice were killed by a rapid injection of saturated KCl solution through a catheter. Various organs, including the tail, were then assayed for their content of ^{86}Rb , a measure of blood flow. The results showed that there was no significant difference between control and irradiated mice in the blood flow in the tail after irradiation under conditions of normal flow. However, in organs with maximal flow, a significant reduction in blood flow was observed in half the tests. The observations supported the idea that damage to the capillaries could be recognized

more easily under conditions of maximal blood flow (De Ruiter, 1975). Invasive methods have been successful in showing changes in the vasculature as a result of irradiation.

2.5.2 Collagen Changes

The injurious effect of irradiation on collagen has not been studied extensively by non-invasive techniques. However, many scientists have shown through invasive methods that collagen levels in the skin increase significantly after irradiation (Autio, 1998; Illsley, 2000; Remy, 1991; Rieki, 2000; and Sarikaya, 1995).

Collagen is the basic structural fiber in all connective tissues. Fifty percent of collagen is made of hydroxyproline, proline, and glycine amino acids. Each collagen molecule is a coiled-coil of three helical polypeptides 290 nm in length. Figure 4 shows the structural formation of collagen. Five molecules align longitudinally with an overlap of approximately one quarter the molecular length to form a microfibril of diameter 3.6 nm causing a banding pattern. The microfibrils are then organized into collagen fibrils which have great tensile strength. The collagen fibrils are surrounded by an extracellular matrix composed primarily of hyaluronic acid with proteoglycans that maintains the integrity and architecture of the collagen (Sarikaya, 1995).

Collagen is a major component of the skin, acting as the main structural component of the dermis layer. The three major types of collagen are I, III, and V. Type I collagen, found in skin, tendon, bone, dentin, ligament, and the cornea, accounts for 90% of body collagen. Type III is frequently found with type I in skin, muscles, blood vessels, cartilage, intervertebral disc, notochord, and the vitreous humor of the eye. Type

V collagen is found in fetal tissues, placenta, interstitial tissues, skin, arteries, uterus, and the intestine. Collagen synthesis takes place in fibroblasts. Irradiation induces the terminal differentiation of cultured fibroblasts, contributing to fibrosis formation (Illsley, 2000).

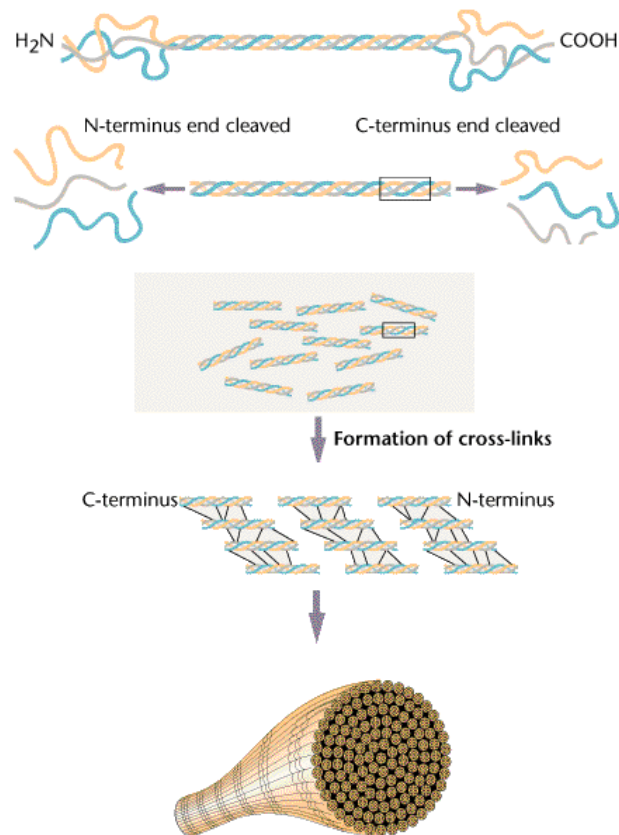


Figure 4. Structural formation of collagen (Griffiths, 2000).

A popular method to evaluate the collagen content in human skin is suction blisters, created with a negative pressure that raises the epidermis and leaves the intact basal membrane on the dermal surface. In order to study in detail the pathogenesis and clinical consequences of irradiation in human skin, Riekkki (2000) and Autio (1998) analyzed collagen synthesis, collagen-degrading enzymes, and the number of active

fibroblasts in irradiated and non-irradiated skin. Autio (1998) induced five suction blisters on the irradiated as well as contralateral breast to obtain suction blister fluid. This interstitial fluid was removed and frozen and the concentrations of carboxy- and amino-terminal propeptides of type I procollagen (PICP) and amino-terminal propeptides of type III procollagen (PIIINP) were determined. This enabled the measurement of collagen synthesis in the skin because as the procollagen propeptides were cleaved off from the extracellular matrix into the interstitial fluid, a collagen molecule was formed. Autio found that the mean concentrations of PICP and PIIINP were about two times higher in the irradiated skin than the contralateral. Figure 5a shows an immunohistochemical staining before radiation where only two PINP-positive fibroblasts are present. However, after radiation (Figure 5b), many more are present. The study also showed that the process of cleaving amino- and carboxy-terminal propeptides from type I procollagen molecules continued despite radiation therapy, which enabled normal binding of collagen molecules into fibers and bundles (Autio, 1998).

Riekkii (2000) published similar results, showing that the mean concentrations of PINP and PIIINP in irradiated skin were respectively 3-5 and 3-4 fold higher than non-irradiated skin. This finding was confirmed by concentrations measured from skin biopsies. The increase in local propeptides did not affect the circulating propeptides, which were within the normal range, further indicating that radiation caused local fibrogenesis (Riekkii, 2000).

A controlled clinical study examined the effect of irradiation on fibroblast collagen synthesis. Fibroblasts from irradiated and non-irradiated sites were cultured in vitro, and collagen production rates were measured using an ultrasensitive high

performance liquid chromatography (HPLC) technique capable of detecting picomolar concentrations of hydroxyproline, an amino acid highly selective for collagen. The study found that collagen production was elevated in cells cultured from irradiated skin. The median collagen production rate was 61.16 pmoles hydroxyproline/105 cells/hour in irradiated cells versus 39.78 pmoles hydroxyproline/105 cells/hour in non-irradiated cells. This suggested that irradiation *in vivo* induced an altered cell phenotype which was subsequently stable in cell culture. This was consistent with the hypothesis that these cells underwent, as a result of irradiation, a stable phenotypic change, a component of which increased or upregulated collagen synthesis (Illsley, 2000).

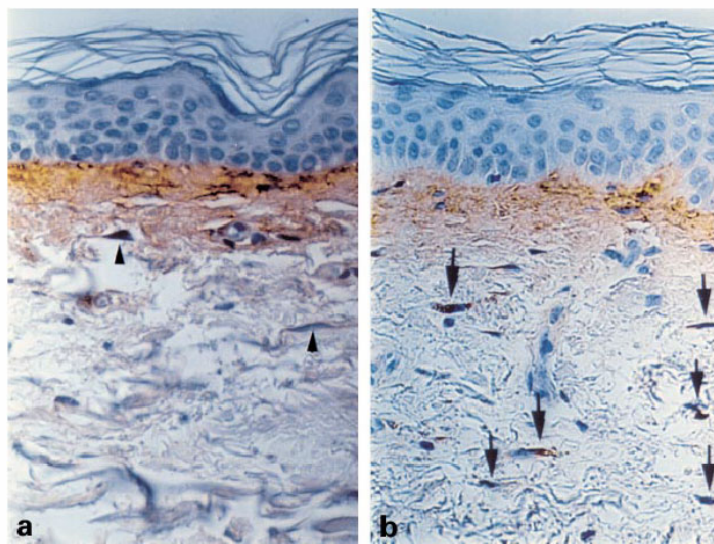


Figure 5. Immunohistochemical staining of human breast skin. The arrows represent the number of PINP-positive fibroblasts (a) before irradiation; and (b) after irradiation (Autio, 1998).

Remy (1991) studied the levels of proteins and mRNA in pig and correlated those with an analysis of collagen synthesis. With the knowledge that a fibrosis scar did not develop like a scar in normal wound healing but remained active for months or years, and

exhibited both an overproliferation of fibroblasts and an overproduction of extracellular matrix, he began to investigate collagen synthesis. He believed that the fibroblast activation resulted from the release of cytokines and growth factors into the tissue by inflammatory cells. By studying the amounts of hydroxyproline in irradiated and non-irradiated tissue, ten times more collagen was measured in the fibrotic tissues than in the normal tissue. Measurements showed that there was seven times more type I and ten times more type III collagen than the normal tissue. The levels of type I and type III procollagen mRNAs were, respectively, nine and five times higher in fibrotic tissue than in normal tissue. Remy (1991) also found that there was an overproduction of fibronectin. The overproduction of fibronectin and type III collagen suggested abnormal regulation of the scarring processes inducing a constant turnover of the immature extracellular matrix for up to 15 months after radiation injury (Remy, 1991). Performing experiments that showed the procollagen or hydroxyproline levels have been popular in evaluating the increase in collagen content after radiation (Autio, 1998; Illsley, 2000; Remy, 1991; Rieki, 2000; and Sarikaya, 1995).

2.5.3 Skin Layer Changes

Many changes in the structure and cell populations of the epidermis and dermis layers are indicators of fibrosis formation. Archambeau (1985) correlated the histological changes that occurred in the dermal microvasculature with the epidermal and endothelial population changes. Single absorbed doses of 1649, 2231, and 2619 rad were applied, the animals were killed for 1-70 days following irradiation, and the whole field was biopsied. The number of epidermal cells intersecting a one centimeter line projected on

the epidermis quantified the changes in population density, in cells/cm, over the 70 day period. The onset of fibrosis was represented by an area of erosion that formed about 17 days post-irradiation. Epidermal cell degeneration with a linear cell loss occurred until day 25. An exponential epidermal cell replacement appeared during the third week and predominated (Archambeau, 1985).

Another theory was that regeneration of the epidermis after radiation was achieved because surviving cells in the basal layer of the epidermis or hair follicles divided rapidly and spread to cover the irradiated area. If new cells were produced very rapidly, some could become piled on top of others. A macroscopic nodule would then be visible, provided that many superficial cornified cells were absent and one could see through to the nodule. The dorsal skin was placed in 25% acetic acid for epidermal separation. The skin was flattened with cornified cells downward on slides and the slides were then exposed for three weeks to produce densely-labeled cells. Day 1 after low doses of radiation showed scattered labeled cells throughout the basal layer, higher doses showed many more labeled cells. After day 2, all doses showed many single scatter labeled cells and groups of several neighboring labeled cells. These groups were believed to be early foci of epidermal regeneration. By day 4, the foci were much larger with many associated labeled nuclei and large average clone areas of nearly 50 percent. The results showed that there were cells in the basal layer capable of apparent rapid exponential cell division during the first few days after irradiation. These cells were shown to divide rapidly so that about half the cells were in the S phase at any one time. The distribution of these cells in fairly homogeneous skin was apparently non-random since there was a clear indication that some clones were associated with hair follicles. In

the mice there was little evidence that macroscopic nodules were formed since the cells appeared to spread and migrate too rapidly (Al-Barwari, 1976).

In order to gather information non-invasively about the skin layers after radiation, Gottlober (2002) used sonography. Concurrently with other imaging techniques, he found that high-frequency 20 MHz sonography could show dermal defects and cutaneous fibrosis, to determine skin thickness in patients with radiation fibrosis, and to evaluate drug effects on the skin (Gottlober, 2000). Many scientists used invasive and non-invasive approaches to show that changes in the structure and cell populations in the epidermis and dermis layers of the skin correlated to the onset and extent of fibrosis (Archambeau, 1985; Al-Barwari, 1976; and Gottlober, 2000).

2.6 Grading Fibrosis Reaction

There are not many existing quantitative methods to assess the onset and extent of fibrosis in skin after irradiation. Most analyses have been qualitative methods, or the use of a word to describe the condition without regard to quantity. In the scientific community, quantitative methods, or those pertaining to numbers and statistics, are more highly regarded. Many methods previously used to grade the extent of fibrosis in the skin are described below.

2.6.1 Qualitative Methods

As early as 1976, scientists tried to quantify the effects of radiation on the skin after cancer treatments. Field (1976) made up an arbitrary system of scoring the acute skin reactions of patients undergoing radiation treatment. No reaction received a score of 0, faint erythema was 1, definite erythema was 2, and marked erythema was 3. When

there was uncertainty between two degrees of erythema, the score halfway between was applied (Field, 1976).

More recently, while irradiating mouse flanks, Iwakawa (2003) created a more complex arbitrary scale to show the reaction of skin to irradiation, as seen in Table 1.

Table 1. Mouse leg skin reaction (Iwakawa, 2003)

Score	Observation
0.5	50/50 doubtful if there is any difference from normal
1-	Definite but slight abnormality
1	Definite abnormality with reddening
1+	Severe reddening and/or white scales and/or puffiness
1.5	Moist breakdown in one very small area, with scaly or crusty appearance
1.5+	Moist desquamation in small areas (more definite than 1.5)
2	Breakdown of large area, possibly moist in places
2.5	Breakdown of large areas of skin with definite moist exudate
3	Breakdown of most of skin with moist exudate
3.5	Complete moist breakdown of limb – often stuck to body

Delanian (1994) and Lefaix (1999) used quantitative and qualitative methods for their analyses. The qualitative scoring showed changes in the density of the irradiated skin. A score of 0 meant no change, a + was a slight but perceptible softening, ++ meant significant softening, and +++ corresponded to a very pronounced softening which indicated that the original zone of fibrosis could barely be distinguished from the surrounding tissues (Delanian, 1994; Lefaix, 1999).

In order to measure subcutaneous fibrosis, Hirota (2002) and Johansen (1994) graded it according to the following scale based on changes: 0 for none, 1 for mild

(palpably increased density), 2 for moderate (definitely increased density and firmness), and 3 for severe (very marked density, retraction, and fixation; hard to pinch the skin) (Johansen, 1994; Hirota, 2002). Side effects that appeared as a result of fibrosis were scored by Hirota as follows: 0 for none, 1 for mild, 2 for moderate (mild contractile pain or uncomfortable feeling that occurred once in a while but did not impair ordinary life), and 3 for severe (severe and continuous contractile pain or uncomfortable feeling sometimes accompanied by impaired mobility). In this study, the scores on the last follow-up date were analyzed in relation to the state of fibrosis (Hirota, 2002).

Another method of grading the degree of fibrosis has been to assess the impairment of movement of the irradiated area. Johansen studied patients with irradiated shoulders and compared maximal abduction and flexion with the normal side, and the degree of impairment was scored on a scale from 0 to 3 (Johansen, 1994).

In a study judging cosmesis, or the appearance of the patient after surgery, the most frequent complaint for patients after radiation therapy for cancer was severe firmness and extensive scars. However, rating cosmesis was subjective. Patients were asked to rate the difference of irradiated and non-irradiated skin in terms of visibility of scars, firmness, and change in color. These questions aimed at the specific radiation consequences such as retraction, atrophy, edema, fibrosis, pigmentation, and telangiectasia. All questions employed a five point response scale with ratings ranging from “excellent” to “very poor” or “none” to “very much,” as appropriate. The impact of specific alterations of the breast on cosmesis was depicted as satisfactory, acceptable, or poor. Using this scale, severe color changes seemed to be more important to patients than doctors, whereas severe fibrosis seemed more disturbing to the doctors. In this

study, doctors rated fibrosis as moderate to severe less frequently than the patients. Patients were more troubled by mild degrees of fibrosis possibly because of functional changes, such as discomfort or sensitivity of the breast. Patients' satisfaction with cosmesis was found to be greater than the doctors'. Severe fibrosis was detected with a high rate of specificity and sensitivity (Hoeller, 2003). Methods of scientists and doctors for grading fibrosis have ranged from using number, plus, and word degree rating systems.

2.6.2 Quantitative Methods

Without an accepted international quantitative classification of fibrosis, Delanian (1994) evaluated the results of treatment with an anti-inflammatory drug. Routine evaluation included palpation of the fibrotic block and determination of the length and width of the projected cutaneous surface. First, the differences in the linear dimensions of the cutaneous surface of the fibrotic zones before and after treatment were calculated. Also, the difference in the area of the cutaneous surface of the fibrotic zone before and after treatment was determined. This non-invasive quantitative data was then correlated with invasive clinical evidence of inflammation (Delanian, 1994).

In a similar experiment, pigs were irradiated with a single dose of 160 Gy and assessed for changes in the density of the palpated fibrotic block and in the dimensions of the projected cutaneous surface. The depth of scar tissue was determined by ultrasound. The density, length, width, and depth of the block of fibrotic scar tissue, and the area and volume of its projected cutaneous surface, were compared. The irradiated field corresponded to a trapezoid shaped zone delimited by the formation of an area of moist

desquamation. Palpation of the irradiated thigh revealed a well-defined block of dense hard fibrosis involving the skin, subcutaneous adipose tissue, and biceps femoris muscle. In this experimental series of pigs, the volume was larger than that of the zone given a high dose of irradiation. However, no changes in fibrotic zone size were observed as a function of time (Lefaix, 1999).

Johansen (1994) used a different approach to quantitatively characterize different degrees of subcutaneous fibrosis after post-mastectomy radiotherapy. A study was performed to assess the value of calculated relaxation times from magnetic resonance (MR) images. A surface coil was applied to the irradiated area, as well as non-irradiated skin, to obtain appropriate MR coronal slices for acquisition of calculated values using a mixed imaging sequence technique. This technique was used since mature fibrosis consists predominantly of dense hypocellular collagen with only a small amount of free water molecules to exchange energy in MR examinations. In addition, arm oedema, or swelling from excessive accumulation of fluid in tissue, was measured quantitatively by the difference between the maximum circumferences of the irradiated and contralateral arms (Johansen, 1994).

Bourgeois (2003) studied breast cancer patients using a quantitative method called cutaneous microrelief, which involved cutaneous imprint processes and image analysis. The following parameters were systematically measured: average roughness of the skin, average furrow depth, residual length, the number of furrows, and the space between furrows. The comparison of the imprints gathered showed a slight increase of skin roughness after radiation. The research showed a significant increase in furrow depth along with an increase in residual length. When the number of furrows did not

significantly decrease, the space between furrows increased (Bourgeois, 2003).

Another correlation was found between the dielectric constant of the skin or subcutaneous fat, and the clinical score for subcutaneous fibrosis. This suggested that the skin dielectric measurement could be a potential tool for assessing skin fibrotic lesions (Lahtinen, 1999). Most quantitative methods to assess the degree of subcutaneous fibrosis have been based on changes in dimensions of the affected area, magnetic resonance (MR) imaging, and changes in range of motion after radiotherapy.

2.7 Thermography

2.7.1 Infrared Light

Thermography is the use of an infrared camera to visualize and measure thermal energy emitted from an object. Thermal, or infrared (IR) energy, is light that is not visible because its wavelength is too long to be detected by the human eye. Sir William Herschel, an astronomer, discovered IR in 1800. He devised an experiment using a prism, paperboard, and thermometers with blackened bulbs where he measured the temperatures of the different colors of the spectrum. Herschel observed an increase in temperature as he moved the thermometer from violet to red in the rainbow created by sunlight passing through the prism. He found that the hottest temperature was actually beyond red light. The radiation that caused this heating was not visible so Herschel termed this invisible radiation “calorific rays.” Today, we know it as IR. Under IR light, everything with a temperature above absolute zero emits heat. The higher the object's temperature, the greater the IR radiation emitted (FLIR, 2002).

The amount of radiated power is proportional to the body's temperature, raised to

the fourth power and determined by the following equation (Kelch, 1998):

$$W = E * B * T^4 \quad (1)$$

where W is the spectral radiant excittance [Watt * cm⁻²], E is the emissivity, B is the Stefan Boltzmann constant (5.67x10⁻¹² Watt cm⁻² K⁻⁴), and T is the temperature in degrees Kelvin. Many scanners and cameras have been designed and produced to visualize light in the IR range.

2.7.2 Thermography Camera

A thermography camera is a non-invasive device that detects infrared energy and converts it to an electronic signal, which is then processed to produce a thermal image on a video monitor where temperature calculations can be performed (FLIR, 2002). Heat sensed by an infrared camera can be very precisely quantified. Infrared thermal imagers capture a portion of the radiated energy and are calibrated to indicate specific temperatures. Thermal cameras are popular because they are completely non-contact, quantify temperature precisely, acquire images quickly (resolution and speed independent) and allow for a large imaging area.

There are currently two types of focal plane array (FPA) imagers: cooled and uncooled. Cooled FPA systems operate in the 3-5 micron or near-infrared range and generally provide excellent sensitivity. The newest FPA imaging systems use uncooled detectors. Unlike previous infrared systems that sensed photons, these microbolometer systems operate by sensing changes in electrical resistance across the detector, produce high-resolution images, but do not require cryogenic cooling systems. Currently, all microbolometers operate in the 8-12 micron or mid-infrared range. The increased

resolution found on FPA microbolometer systems enables users to discern minute temperature variations and provides highly accurate temperature readings (FLIR, 2002). Commercial infrared imagers are not manufactured in the 5-8 micron range due to atmospheric absorption of infrared energy at these wavelengths.

2.7.3 Static Thermography

Thermography graphically depicts temperature gradients over a given body surface area at a given time. It has the ability to study biological thermoregulatory abnormalities that directly or indirectly influence skin temperature (Maxwell-Cade, 1968; Head, 2002). Through a variety of scanning techniques a spatial map of temperatures called a thermograph or thermogram is created, as shown in Figure 6. Regions of high temperature are seen as dark red and white shades.

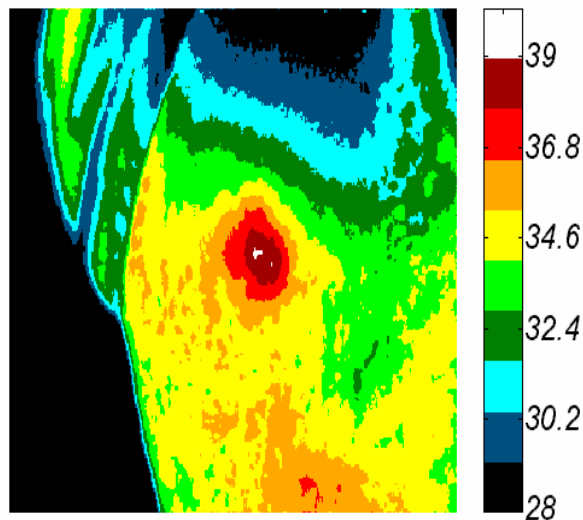


Figure 6. Thermogram of left shoulder and back of patient with a vascular tumor (Kaposi's Sarcoma Protocol, NCI, NIH).

However, skin temperature is only an indirect measure of skin blood flow (Love, 1980).

In fact, the superficial thermal signature of skin is related to metabolism and vascularization within the underlying tissues. Temperature measurement is the most widely used technique for the evaluation of skin circulation (Usuki, 1998). It may therefore change significantly as a result of pathological processes. Since radiation has been shown to cause vascular changes in the skin, thermography should be evaluated as a non-invasive analysis tool.

2.7.4 Time-Response Thermography

Since damage to the skin alters the thermoregulatory response of the injured area with respect to healthy ones, Merla (2002) believed that thermography could be a useful way to detect these changes. However, the informative content of static infrared images was limited to the observation of thermal skin distribution and to the identification of possible asymmetries with respect to a mean behavior obtained from a reference sample. Merla performed a cold stimulation on the suspect damaged area and its surroundings assuming that affected areas would have a faster or slower recovery time based on the disease. This experiment was tested on muscular lesions, Raynaud's phenomenon secondary to scleroderma, and vein thrombosis.

Measurements were obtained in a temperature- and humidity-controlled room. To perform the movement correction of the acquired series of images, paper markers were put on the body surface of the subject corresponding to anatomical reference points. Ten images were acquired and averaged as a basic reference before the thermal stress; then, another 40 images were acquired after the thermal stress at an interval of every 30 seconds. The thermal stress was performed through a cold dry patch, 10 °C below the

basal skin temperature, applied for two minutes on the damaged area and its surroundings. Analysis of the data included movement correction, and evaluation of the thermal recovery and Tau time. Tau time was the time to recover following the cold stimulation, which was 63% of ΔT , since the re-warming curve seemed to closely resemble an exponential behavior. The formula to calculate 63% ΔT was:

$$63\% \Delta T = (T_i - T_0) * 0.63 + T_0 \quad (2)$$

where T_i was the average temperature of the images taken pre-stimulation, and T_0 was the temperature of the image taken immediately after the cold stimulation was removed (Frame 1).

A region of interest (ROI) was selected on the movement-corrected series of images, the time evolution of the thermal recovery exhibited by each pixel of the ROI was obtained and the associated Tau time was evaluated. The static thermographic image on the left of Figure 7 shows almost identical distribution of heat through both hands. However, the Tau image after cold stimulation shows a non-homogeneous distribution of reheating times.

If the disease featured an associated blood shedding, an inflammatory state, or increased blood flux, Merla showed it exhibited a faster recovery time with respect to the surroundings and a smaller Tau value. In contrast, in presence of localized calcifications, early ulcers or scleroderma, the damaged areas showed a slower recovery than the healthy surrounding areas. Similarly, the presence of Raynaud's phenomenon resulted in a very slow thermal recovery, especially in the exponential phase of the re-warming. This was probably due to a change in the thermal capacity of the tissue.

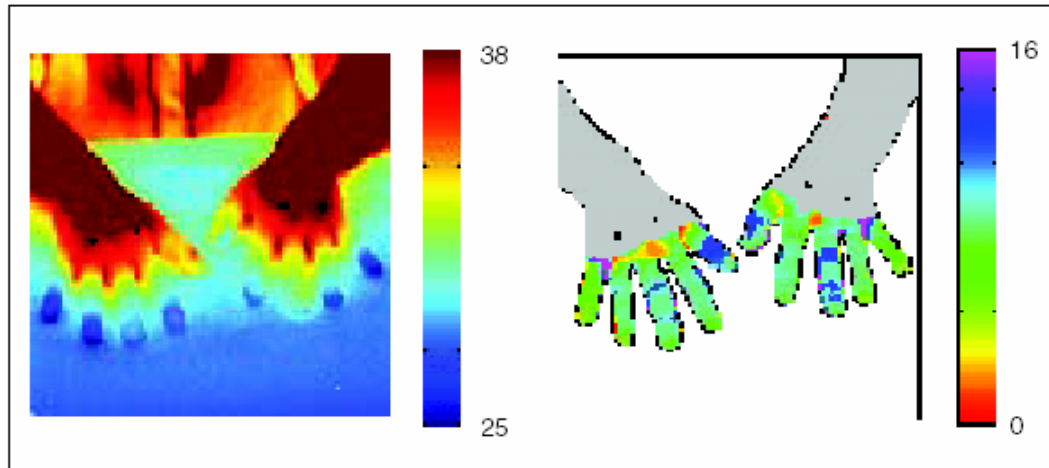


Figure 7. Static thermographic image and Tau image of Raynaud's phenomenon secondary to scleroderma (Merla, 2002). The colorbar shows the recovery time in minutes of each image pixel. The areas associated with longer recovery times (blue) identify with the main damaged areas.

This technique allowed objective evaluation of the effectiveness of rehabilitative therapy, since it provided information about the tissue repairing process independently of the patient indications and in agreement with ultrasonography reports. Therefore, it could be used in the follow-up of specific therapies, or in the evaluation of the effectiveness of drugs able to produce local effects on the skin thermoregulation (Merla, 2002).

2.8 Laser Doppler Imaging

2.8.1 Laser Doppler Imaging Technique

The laser Doppler technique measures blood flow in the very small blood vessels of the microvasculature (Moor-LDI, 2002). The tissue sampled is typically one millimeter thick, capillary diameters are ten microns, and the velocity spectrum measurement is typically 0.01 to 10 mm/s. The theory of the Doppler technique, shown in Figure 8, begins when low power light from a monochromatic stable laser, such as a 5-

mW Helium-Neon laser, incident on tissue, is scattered by moving red blood cells. The frequency-broadened light, together with laser light scattered from static tissue, is photodetected and the resulting photocurrent is processed to provide a blood flow measurement. The term commonly used to describe blood flow measured by the laser Doppler technique is flux. Flux is expressed in arbitrary perfusion units and is a quantity proportional to the product of the average speed of the blood cells and their number concentration, often referred to as blood volume.

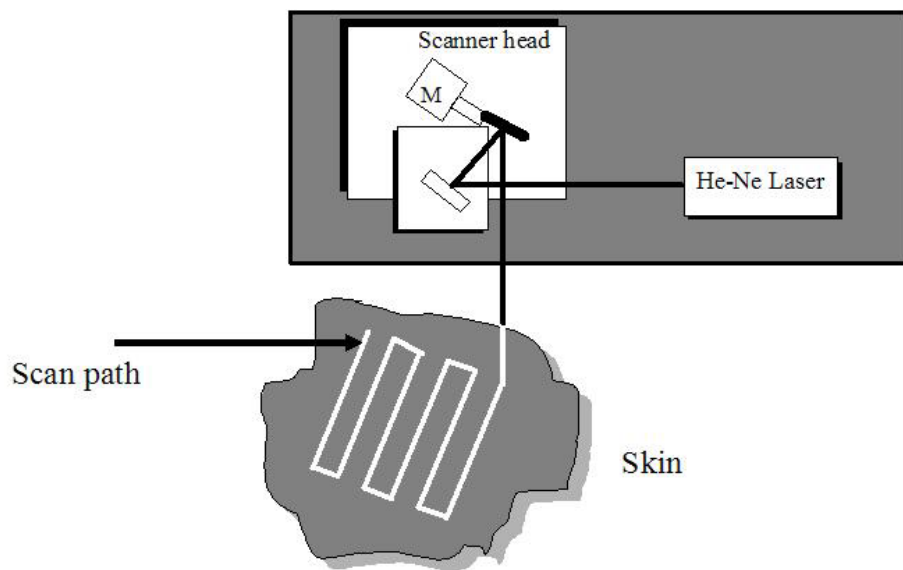


Figure 8. Laser Doppler imaging technique.

2.8.2 Laser Doppler Imaging Applications

Laser Doppler imaging (LDI) measures the Doppler shift due to the movement of red blood cells. The signal reflects the product of the velocity of red blood cells and the number of light-cell interactions. LDI enables non-invasive analysis of blood flow patterns in skin up to an approximate depth of one millimeter. It can register flow in a variety of vessels including arterioles, capillaries, and venules. Each laser Doppler image

measures blood flow distribution in the superficial layer of skin. Areas are scanned enabling the blood flow to be mapped and color coded images of the blood flow to be displayed. Figure 9 shows that highly vascular areas can be detected from the surroundings. Laser Doppler imaging visualizes diseased states which exhibit highly vascular areas, such as tumors. Regions of interest can be defined and statistical data can be calculated and recorded.

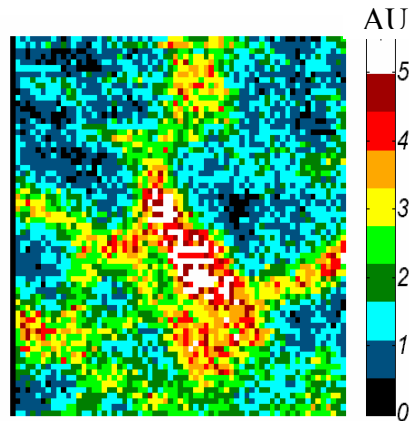


Figure 9. Laser Doppler image shows blood flow through veins (Kaposi's Sarcoma Protocol, NCI, NIH).

2.9 Near-Infrared Multi-Spectral Imaging

2.9.1 Near-Infrared Multi-Spectral Imaging Technique

The multi-spectral imager contains a charge-couple device (CCD) detector (Roper, 2003) that captures images at six wavelengths in the near infrared (NIR) range (700, 750, 800, 850, 900, and 1000 nm) by using a rotating filter wheel. NIR wavelength light is chosen due to tissue's low absorption in the NIR allowing for increased tissue penetration. The schematic is shown in Figure 10.

To further increase the penetration of the detected light, polarization filters selectively filter light that only scatters a few times. One filter is placed in front of the

light source and another in front of the CCD camera and both are set up to be cross-polarized. Thus, light scattered from shallow tissue exhibiting very short photon path lengths is blocked and the more scattered light depolarizes and is detected. The controller controls the camera and the six different wavelength images are sent to the computer.

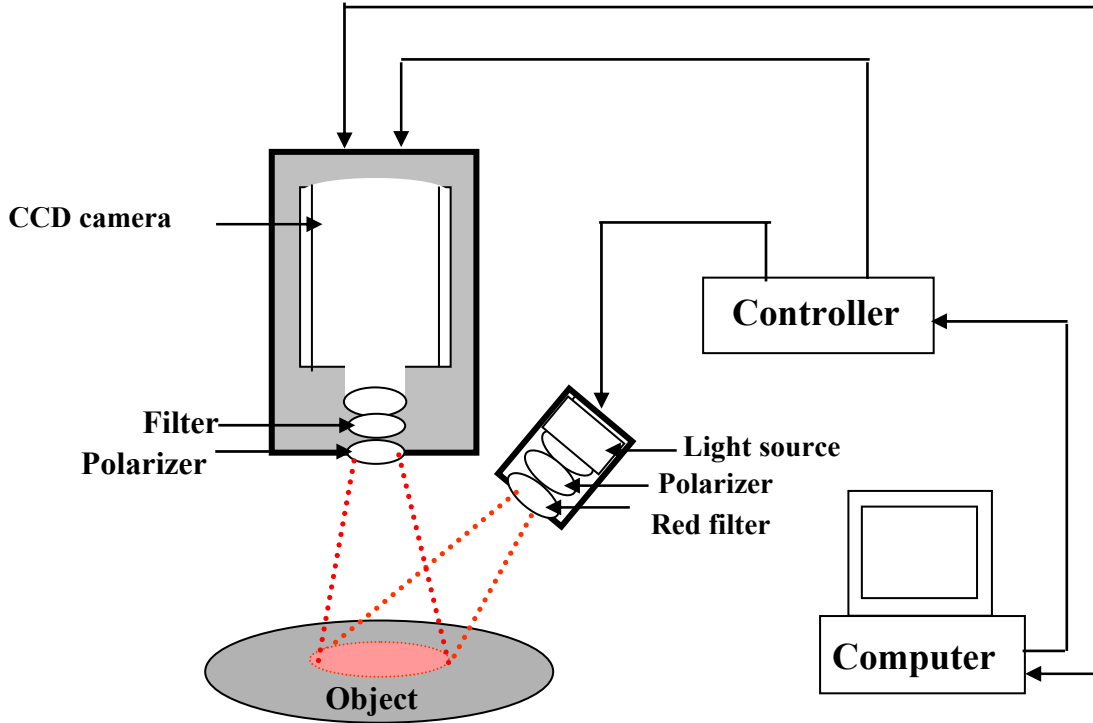


Figure 10. Schematic of the near-infrared multi-spectral imaging system. The filter wheel in front of the CCD camera contains six filters of 700, 750, 800, 850, 900, and 1000 nm.

2.9.2 Near-Infrared Multi-Spectral Imaging Applications

Light spectroscopic methods are critical to advances in molecular characterization of disease processes. However, these methods have been limited to in-vitro or cell culture studies. In fact, strong scattering in almost all tissue types causes dispersion of

the photon paths which results in poor localization and resolution. Hence, quantitative analysis of spectral data obtained from structures below the tissue surface requires accounting for scattering. Scattering affects both the penetration of the photons and the path length over which the photons are subject to molecularly specific absorption. The goal of much current research is to non-invasively obtain diagnostically useful molecular information from embedded sites (Hattery, 2002).

Figure 11 shows a typical result of spectral analysis for a patient with vascular tumors. The reconstructed images for the oxy-hemoglobin levels are shown. In the top reconstructed image, lesion 5 does not show high oxy-hemoglobin levels like lesion 1. The contralateral area (bottom reconstructed image) shows a value of nearly zero throughout.

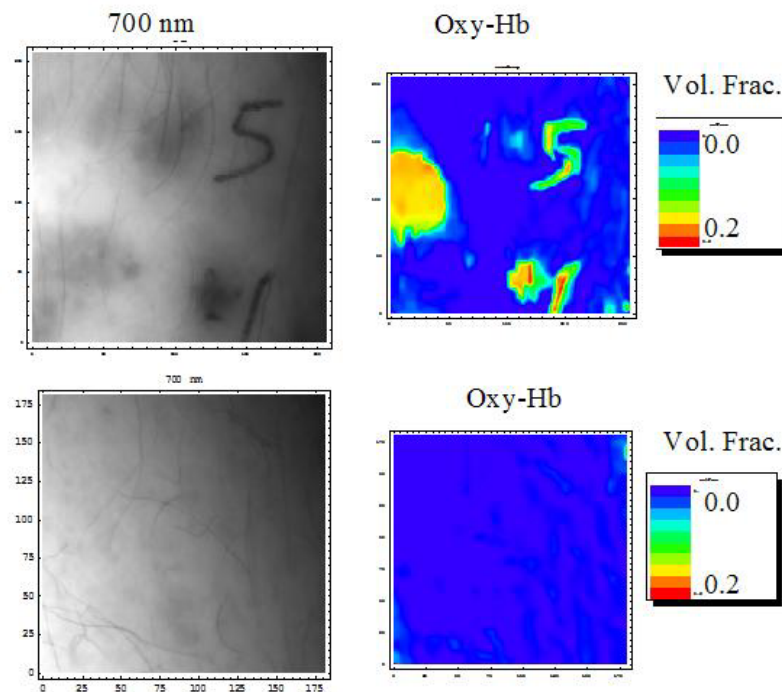


Figure 11. 700 nm spectral and oxy-hemoglobin fraction images. The top image shows a lesion area and the bottom image shows a contralateral lesion-free area (Kaposi's Sarcoma Protocol, NCI, NIH).

Chapter 3: Objectives

The major goal of this research was to quantitatively analyze the effects of radiation on mouse tissue using non-invasive imaging techniques. The radiation damage to the skin has been thoroughly investigated by invasive techniques. The onset and extent of fibrosis have been graded according to numerous qualitative and quantitative methods. This research utilized two non-invasive imaging techniques: thermography and near-infrared multi-spectral imaging. Time-response thermography was used to determine if the thermal characteristics of the skin changed after radiation by showing the skin's response to cold stimulation. Laser Doppler imaging monitored the blood flow before and after the cold stimulation. Near-infrared multi-spectral imaging monitored changes in the oxy-hemoglobin fraction and blood volume after radiation.

The specific objectives were to:

1. Determine with thermography if there was a faster or slower thermal recovery time after cold stimulation pre- and post-irradiation.
2. Determine through laser Doppler imaging analysis if there was a change in blood flow before and after the cold stimulation.
3. Determine if there were differences in oxygen blood fraction and blood volume before and after radiation and between irradiated and non-irradiated mice.

Chapter 4: Materials and Methods

4.1 Mice

4.1.1 Mouse Selection and Care

NCr athymic nude female mice (14 weeks old) obtained from the National Cancer Institute at the National Institutes of Health were selected after experiments were conducted with hairy mice. Before each experiment, the hair in the irradiated area was removed from the right flank by using hair removal lotion and plucking remaining hairs. The hair removal was necessary for the near-infrared multi-spectral imaging reconstruction. Since this process was time-consuming and not perfect, nude mice were instead selected.

Nude mice, as seen in Figure 13, have a mutational defect that results in the animal having hair at birth and by day 21, all hair on the body is lost and the hair follicle atrophies. Athymic mice lack a normal thymus gland, and have a defective immune system because of a genetic mutation. Athymic nude mice are often used in cancer research because they do not reject tumor cells, from mice or other species.



Figure 12. NCr athymic nude immunocompromised female mouse (<http://www.aceanimals.com/AthymicNudes.htm>).

The mice were randomized into control and radiation groups. Each mouse was labeled on day 0 so that it was identifiable during the experiment. The mice were housed in cages by individual radiation dose levels and had free access to food and water. They were kept at a room temperature of 22-25 °C with 12 hours of light and 12 hours of dark per day.

For many reasons, this research studied twelve mice: five control, three 30 Gy, two 32 Gy, and two 35 Gy. The mice in this experiment had to be old enough (at least 14 weeks old) and large enough to limit their movement in the plexiglass holder (Figure 14). After the experiments began, there were outbreaks of several viruses in the animal facility where the mice were housed. First, a skin virus spread through the animal facility and the mice could not be used. Since skin was the only tissue imaged in this study, the data would not be reliable if the skin was affected by disease. More recently, a deadly mouse virus spread through the animal facility and all of the mice had to be euthanized. Preliminary data collected from mice receiving radiation doses of 20, 25, and 40 Gy also utilized the available supply. The initial mice were helpful in creating better methods but could not be used in the final results of this thesis. In alignment with the Animal Use and Care Committee, twelve mice were chosen as the sample size for this experiment.

4.1.2 X-ray Irradiation Procedures

Mice flanks were irradiated with a single dose of X-ray irradiation of one of the following: 30, 32, or 35 Gy. To perform the irradiation procedures, fully awake mice were restrained in specifically designed jigs that provided protection to the mouse's body and yet permitted exposure of a 1 x 2 cm rectangular flap of skin. Each mouse was

placed under a 300kV, 10mA radiation beam for a designated amount of time based on a 207 rad/min conversion. Upon completion of irradiation, the mice were removed from the jigs and put back into their bonneted cages and taken out of the animal facility and moved to the imaging laboratory (Russo, 2002).

The radiation doses were selected after preliminary experiments were conducted with 20, 25, and 40 Gy doses. The acute skin damage from radiation, including desquamation and the appearance of red, crusty skin after two weeks, could not be seen with the low doses of 20 and 25 Gy. A single dose of irradiation at those levels was not enough to see the skin reactions required for this research. Subsequent experiments with a dose of 40 Gy were conducted; however, the dose level killed a majority of the mice before the second week of imaging could be completed. Therefore doses 30, 32, and 35 Gy doses were selected for this research.

The X-ray irradiation machine was run for 14 minutes and 29 seconds, 15 minutes and 27 seconds, or 16 minutes and 54 seconds for 30, 32, and 35 Gy doses respectively. After initial experiments, it became necessary to place fiducial marks on the mouse skin before irradiation. The India ink tattoos had to last for two months as well as not bleed or travel underneath the skin. Since the tattoos were placed just under the mouse skin in the irradiated area, the irradiated area could be compared throughout the study.

4.1.3 Plexiglass Holder

To take accurate images, movement had to be limited for the entire experimental procedure, but the mice could not be anesthetized because the blood flow would drop significantly after applying an anesthetic. To keep the mouse from moving, the mouse

was placed in a plexiglass holder designed and manufactured for this research (Figure 14). The holder was created with open spaces on the irradiated and contralateral control areas to allow for imaging.

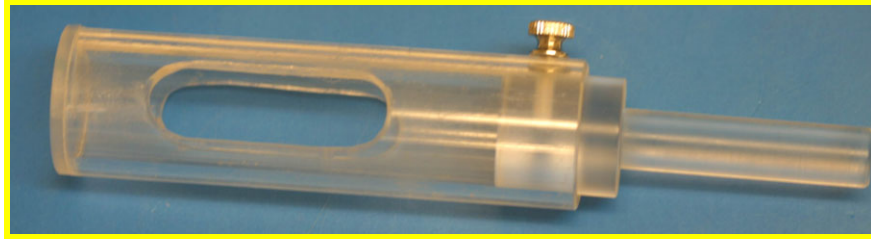


Figure 13. Plexiglass holder designed and manufactured to decrease movement of mice during imaging.

The hind legs and tail of each mouse were taped down against the holder, as shown in Figure 15, so that the mouse could not escape. Cotton gauze was placed at the right of the holder underneath the rear end of the mouse in order to allow the irradiated area to show in the open window. This holder, along with image registration, decreased movement during the experimental procedures.



Figure 14. Plexiglass holder with mouse legs and tail taped down for limited movement.

4.2 Imaging Procedures

In order to achieve the objectives, measurements were taken before irradiation and up to eight weeks after irradiation.

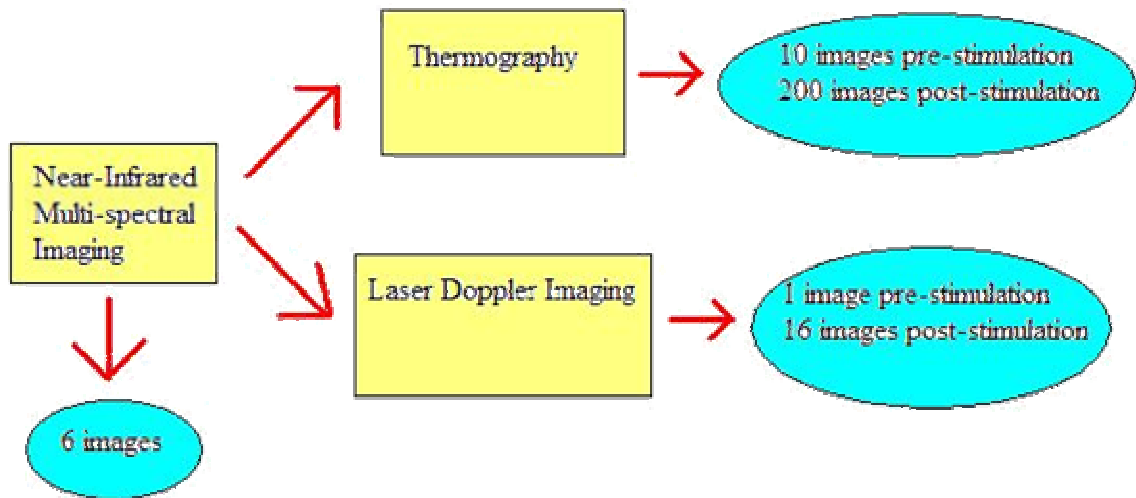


Figure 15. Block diagram of three imaging techniques (near-infrared multi-spectral imaging, thermography, and laser Doppler imaging) and images collected during each experiment.

First, six near-infrared multi-spectral images were collected at wavelengths 700, 750, 800, 850, 900, and 1000 nm. Then, before the cold stimulation was performed for one and a half minutes, thermal and laser Doppler images were collected simultaneously. Ten thermal images were averaged while one laser Doppler line scan image was collected. After the cold stimulation, sequences of 200 thermal and 16 laser Doppler images were collected. The details of the experimental procedures and methods of analysis are described in greater detail below.

4.3 Thermography

4.3.1 Thermal Camera

For this study, images were taken using the Thermovision Alert SC500 camera (Figure 16). The 3-5 micron camera owned by the laboratory was not selected for these experiments because it did not have the capability of taking a sequence of pictures. FLIR

Thermacam Researcher software was purchased for its ability to take a sequence of images. All of the thermal imaging analysis was performed using MATLAB 6.5 including the Image Processing Toolbox.



Figure 16. Thermovision Alert 8-12 micron thermal camera (SC500) (FLIR, 2002).

4.3.2 Thermography Procedure

Initial experiments that utilized thermography as a method to visualize the irradiation effects on skin showed that full size images did show enough resolution of the small irradiated area. Also, variations in average mouse temperatures and thermal heterogeneity of the mouse flank (Figure 17) made it difficult to compare static temperature averages alone. These preliminary studies and previous experiments (Merla, 2002) showed that calculating the thermal recovery to cold stimulation might yield better results, as compared to using the full size thermal images.

A cold stimulation time-response experiment was performed on the mice because after the skin was irradiated, the skin was expected to exhibit different properties. The dynamic study was performed to see different responses of radiated and normal skin to cold stimulation. First, ten images of the right flank area were taken pre-stimulation using the 8-12 micron wavelength thermal camera. Then water was chilled with ice and the cold water was placed inside of a latex rubber tube closed off on both ends. The

rubber compress was placed flat against the mouse flank skin for 1 minute, 30 seconds which changed the skin surface temperature approximately 7-10 °C. Then a sequence of 200 thermal images was captured for 15 minutes at an interval of five seconds.

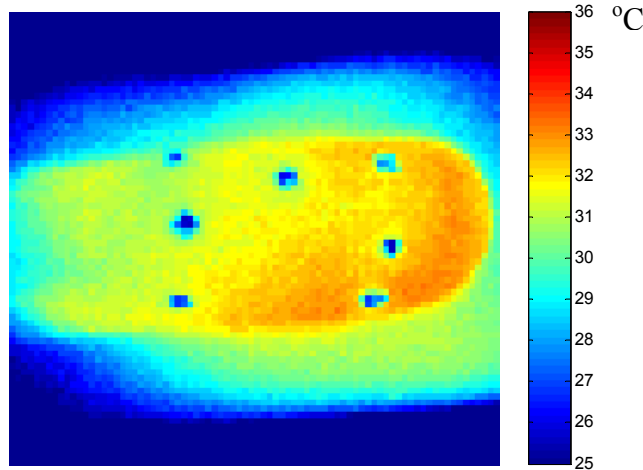


Figure 17. Static thermal image shows the temperature heterogeneity of a control mouse. The control mouse varies in temperature from 30-34 °C. The area on the left of the control mouse, closer to the leg, was generally cooler than the center area, which was cooler than the area on the right, closer to the head.

4.3.3 Preliminary Analyses

The first analysis calculated the time for the tattooed area to reach its pre-stimulation temperature. The main problem with this method was that the irradiated area did not always return to its initial temperature. One reason for this outcome could have been room variability. The initial experiments (day 0) had to be performed in the animal facility and then the mice were moved to a laboratory for the remainder of the study. Both rooms were not temperature- nor humidity-controlled. These environmental changes could have affected the mouse's ability to re-heat fully to its pre-stimulation temperature.

Another method selected a five pixel by five pixel square area to the left, to the

right, and in the center of the tattooed area. Then the change in temperature (ΔT) was calculated by subtracting Frame 100 after stimulation from the averaged pre-stimulation temperature. A similar ΔT was calculated by subtracting Frame 50 from the averaged pre-stimulation temperature. Due to movement of the mice during the experiments, it was difficult to select the exact same 25 pixel square area before and after the cold stimulation. This could have led to error in the calculated means. Also, due to the heterogeneity of the three selected areas (Figure 17) and differences in metabolic processes and responses to radiation, this method showed random differences in the control mice as well as before and after radiation of the radiated mice. Therefore, selecting small pixel areas was not an accurate average for the three distinct regions. On the other hand, selecting a large ROI and averaging the values caused a larger standard deviation.

Similarly to Merla (2002), the time at which 63% ΔT was reached was also calculated by Equation 2 as a method of analysis. 63% ΔT was chosen as the time when the thermal recovery ceased an exponential increase and began to plateau. The calculation showed no significant differences between the time to reach 63% ΔT for the control and radiated mice throughout the experiment. After further literature review, it was realized that Merla knew the cold base temperature and the temperature of his cold patch, which stayed constant. The skin was cooled down to a specific temperature and then the response curve was calculated. At 63% ΔT , the curve ceased to be exponential and began to plateau. However, in the current experiment, the cold stimulation was based on time. The mouse was always cooled for 1 minute, 30 seconds. Therefore, each mouse began at a different base cold temperature causing Merla's analysis technique to

be ineffective.

The slope of the re-heating process was also calculated for a five pixel by five pixel square area in each of the three areas for the first 100 frames after the cold stimulation. The major difficulty with analyzing the sequence of 100 thermal images was movement. For this method of thermal analysis, it was necessary to register the images. In order to calculate a correct slope for 100 frames after the cold stimulation, the same exact area had to be selected for each thermal image frame. Without registering the images, this was nearly impossible. However, registering the images was time consuming for 100 frames and was not exact to the pixel. After registering the images and recording the slopes in the three areas, this analysis did not yield significant differences between the slopes of the radiated and non-irradiated areas during the experiments (Figure 24).

4.3.4 Final Selected Analysis

After the above preliminary analyses were completed, a method that yielded significant results was determined. The method involved calculating the degrees remaining for the three areas to return to their pre-stimulation temperatures at a specifically chosen time point.

A region of interest (ROI) was selected as large as possible for the center tattooed area, as well as the areas to the left and right of the tattooed area (Figure 18). However, only a small portion of the flank could be irradiated (approximately 1 cm x 2 cm), which left for very small regions outside the radiated area to compare as non-irradiated areas. Nonetheless, average temperatures of the three areas were recorded before stimulation

and at the halfway (Frame 100, 8.25 minute) point. Due to constant movement of the mice during the experiments, independent ROIs were chosen for the two frames.

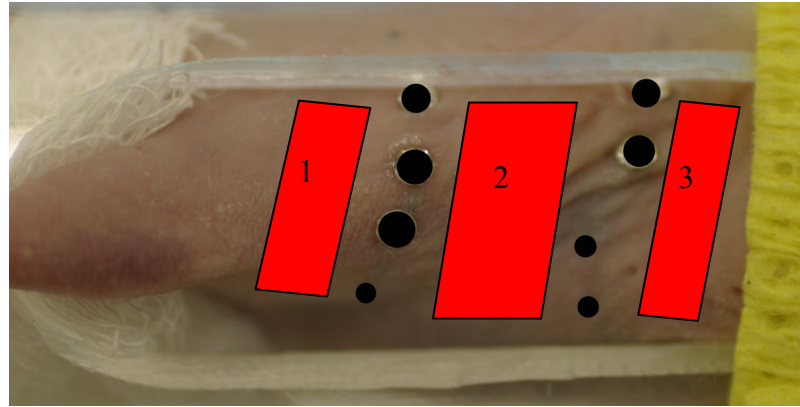


Figure 18. Digital image of mouse shows the three ROIs selected for thermal imaging analysis: (1) Left, non-irradiated area; (2) Center, irradiated area; and (3) Right, non-irradiated area.

The difference in temperature was calculated between Frame 100 and the initial average temperature pre-stimulation. This temperature difference was recorded for all three areas shown in Figure 18. Then the temperature differences were normalized to the center tattooed area. A t-test was performed to find significance between the differences of the left and right sides from the center between day 0 and day 1, week 1, week 2, and week 3.

4.4 Laser Doppler Imaging

4.4.1 Laser Doppler Imager

In the laser Doppler blood flow imager, the low intensity laser beam is scanned across a tissue surface using a moving mirror. The imager is able to map tissue blood flow over areas of 25 cm x 25 cm in 4.5 minutes with 256 x 256 pixel resolution; each pixel being an actual measurement. The moorLDI-2 λ dual wavelength perfusion imager (Figure 19) offers scanning at two different wavelengths for assessing flow from

differing microvascular beds. The laser wavelengths are visible red (690 nm) and near IR (780 nm). There is no direct contact with the tissue being assessed (Moor-LDI, 2002).



Figure 19. Laser Doppler imager (moorLDI-2 λ) (Moor-LDI, 2002).

4.4.2 Laser Doppler Imaging Procedures

For this research, laser Doppler imaging was selected to quantitatively assess if the blood flow changed after applying the cold stimulation. Laser Doppler line scan images were captured consecutively with the thermal images using a laser Doppler imager (Moor-LDI, 2002). Preliminary studies showed that full size laser Doppler images of the entire radiated area could not be used because the resolution was too low. Therefore, only a very small area, approximately 30 x 7 pixels was selected for imaging.

One laser Doppler image was taken before the cold stimulation. After the cold stimulation, images were acquired at an interval of every 30 seconds for five minutes.

4.4.3 Laser Doppler Imaging Analysis

All images were captured and processed using Moor LDI Software. The images were analyzed using MATLAB 6.5 including the Image Processing Toolbox.

For analysis, a mean of the entire line scan image was compared before and after the radiation. Since the entire area imaged was inside the radiated area, a comparison between the radiated and non-irradiated areas could not be made. Laser Doppler imaging only monitored the blood flow in the mouse skin after the cold stimulation.

4.5 Near-Infrared Multi-Spectral Imaging

4.5.1 Near-Infrared Multi-Spectral Imager

In collaboration with the Lawrence Livermore National Laboratory, a multi-spectral imager was designed and built (Figure 20).



Figure 20. Near-infrared multi-spectral imager.

The resolution of each spectral image is 512 by 512 pixels with a maximum area of 5 cm by 5 cm. The near-infrared multi-spectral images were collected before the cold stimulation, to make sure no residual effects of that procedure were observed. The six images collected showed the light intensity at six different wavelengths (700, 750, 800, 850, 900, and 1000 nm). Figure 21 shows an example of a multi-spectral image.

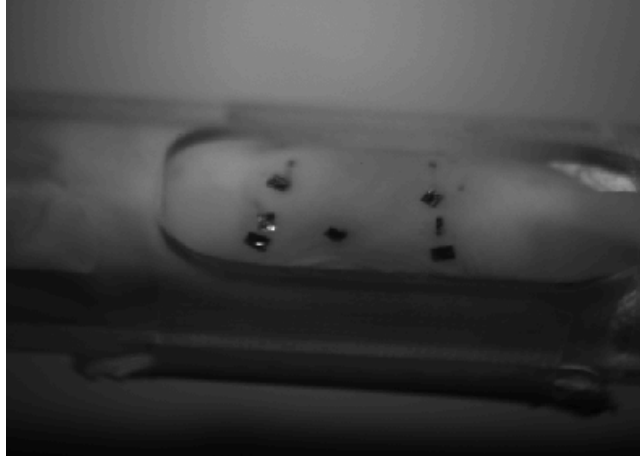


Figure 21. 850 nm near-infrared multi-spectral image of mouse.

4.5.2 Near-Infrared Multi-Spectral Imaging Analysis

Two-layer model-based diffuse reflectance spectroscopy reconstructed for oxy-hemoglobin fraction and total blood volume parameters (Hattery, 2002). In order for the light to be detected, the source light first passed through the epidermis, then the dermis where it reflected back through the epidermis and was detected. The spectral signatures of analytes such as oxy- and deoxy-hemoglobin were known. To obtain information about the analyte concentrations, however, the diffuse reflectance NIR images had to be corrected for scattering. The scattering was modeled using analytical solutions developed from a random walk model of photon migration in turbid media (Gandjbakhche, 1995). When the spectral data was fit to the model, blood volume and blood oxygenation were obtained.

Blood volume and blood oxygen saturation have been generally believed to change after radiation and were therefore of direct interest as indicators of radiation damage. The absorption of blood was a function of the volume fraction of oxy- and

deoxy-hemoglobin. The relative absorption spectra for oxy-hemoglobin, $\mu_{a(\text{oxy})}(\lambda)$, and deoxy-hemoglobin, $\mu_{a(\text{deoxy})}(\lambda)$, are shown in Figure 22 (Hattery, 2002).

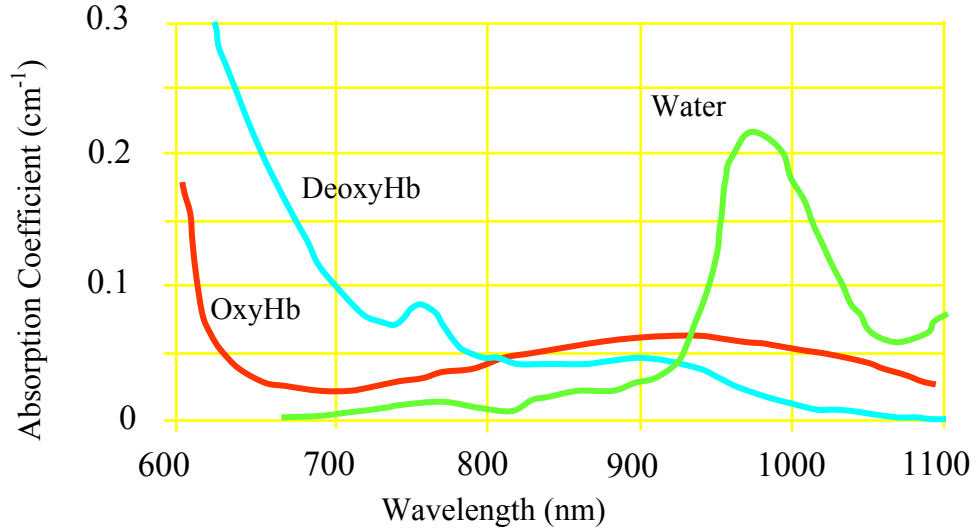


Figure 22. Absorption coefficient spectra for oxy- and deoxy-hemoglobin, and water.

The total blood absorption, $\mu_{a(\text{blood})}(\lambda)$, was expressed as a combination of oxy-hemoglobin and deoxy-hemoglobin (Hattery, 2002):

$$\mu_{a(\text{blood})}(\lambda) = V_{\text{oxy}}\mu_{a(\text{oxy})}(\lambda) + (1 - V_{\text{oxy}})\mu_{a(\text{deoxy})}(\lambda) \quad (3)$$

where V_{oxy} was the volume fraction of oxy-hemoglobin, and $\mu_{a(\text{oxy})}$ and $\mu_{a(\text{deoxy})}(\lambda)$ were the absorption coefficients of oxy- and deoxy-hemoglobin (cm^{-1}) respectively.

Each of the band-pass filters on the imager had a full width at half max (fwhm) of 50 nm. Before using the absorption data for reconstruction, the data had to be convolved with the response function of the band-pass filters. This smoothed the data and removed much of the detail, particularly the deoxy-hemoglobin response near 760 nm shown in Figure 22. For light to reach the dermis it had to first pass through the epidermis. This transmission was a function of the melanin in the epidermis and the epidermal thickness.

All other skin analytes were combined into a single absorption variable $\mu_{a(\text{skin})}(\lambda)$ which was a function of the wavelength. The dominant chromophores in that spectrum were lipids and water. Knowing the absorption spectra of the various analytes, the total absorption in the epidermis was expressed as (Hattery, 2002):

$$\mu_{a(\text{epi})}(\lambda) = V_{\text{mel}} \mu_{a(\text{mel})}(\lambda) + (1 - V_{\text{mel}}) \mu_{a(\text{skin})}(\lambda) \quad (4)$$

where V_{mel} was the volume fraction of melanin, $\mu_{a(\text{mel})}(\lambda)$ was the absorption coefficient of melanin, and $\mu_{a(\text{skin})}(\lambda)$ was the absorption coefficient of skin. The few epidermal scatterings were shallow angle and the transmission through the layer was considered to be independent of scattering. The attenuation through the epidermis was (Hattery, 2002):

$$A_{\text{epi}}(\lambda) = e^{-\mu_{a(\text{epi})}(\lambda)t} \quad (5)$$

where t was the epithelial thickness and $\mu_{a(\text{epi})}(\lambda)$ was the absorption coefficient of the epidermis. To address the air-tissue interface specular reflection, the source and detector had cross polarized filters to block specularly reflected photons. In practice, these two components were accounted for by a scalar intensity scaling factor in the model. The underlying dermis layer was assumed to be infinitely thick and the light passing from the epidermis was no longer collimated due to epidermal scattering. The reflected attenuation from the dermis was (Hattery, 2002):

$$A_{\text{refl}}(\lambda) = \frac{1 - e^{-\sqrt{24\mu_{a(\text{derm})}(\lambda)/\mu_s'(\lambda)}}}{\sqrt{24\mu_{a(\text{derm})}(\lambda)/\mu_s'(\lambda)}} \quad (6)$$

where (Hattery, 2002):

$$\mu_{a(\text{derm})}(\lambda) = V_{\text{blood}} \mu_{a(\text{blood})}(\lambda) + (1 - V_{\text{blood}}) \mu_{a(\text{skin})}(\lambda) \quad (7)$$

and $\mu_s'(\lambda)$ was the transport-corrected scattering coefficient, $\mu_a(\text{blood})(\lambda)$ was the combined absorption coefficient of oxy- and deoxy-hemoglobin and $\mu_a(\text{skin})(\lambda)$ was the absorption coefficient of the skin. Equation 8 is the integrated intensity over the entire plane for point illumination. In practice, intensities at single pixels were looked at as a given illuminance over the entire plane. Then the intensity detected by the camera was expressed as follows (Hattery, 2002):

$$I_{\text{detected}}(\lambda) = c I_s(\lambda) d(\lambda) 2 A_{\text{epi}}(\lambda) A_{\text{refl}}(\lambda) \quad (8)$$

where $d(\lambda)$ was the spectral response of the camera, I_s was the intensity of the source, and c was the intensity scaling factor. The product of $d(\lambda)$ and $I_s(\lambda)$ was generally combined into a single calibration function for the imaging device. The six spectral bands of the imaging system allowed for the reconstruction of up to six unknowns. As a result, the relative differences in reconstructed analyte concentrations acted as the potential indicator of radiation effects (Hattery, 2002).

For the analysis, the images were analyzed to see if the area of irradiation could be clearly visualized in the reconstructed images. A ROI in the irradiated area was selected and mean values of blood oxygen fraction and total blood volume were determined throughout the study.

Chapter 5: Results and Discussion

5.1 Thermography

5.1.1 Changes in Thermal Recovery Times

The difference in temperature was calculated between Frame 100 (8.25 minutes) after the cold stimulation and the average temperature before the cold stimulation. Frame 100 was chosen because preliminary data showed most of the control mice had recovered to their initial temperatures. This temperature difference was recorded for three locations: the tattooed area, to the left of the tattooed area, and to the right of the tattooed area, as shown in Figure 18. Then the temperature differences were normalized to the center tattooed area in order to provide a standardized comparison before and after radiation. Figure 23 shows the temperature differences on day 0 and week 2 for four mice (two controls and two irradiated).

The graph shows that the left and right areas of the control mice re-heated to within ± 0.2 °C of the center area on both day 0 and week 2. The same was true for day 0 of the radiated mice. Conversely, the left and right areas of the irradiated mice at week 2 exhibited temperatures 0.5–0.8 °C higher than their original temperatures when compared to the center. This showed that the irradiated area was always closer to its original temperature than the non-irradiated areas 8.25 minutes after the cold stimulation and exhibited a faster re-heating rate than the left and right non-irradiated areas. The irradiated mice exhibited significant temperature differences from day 0 between the non-irradiated areas and the irradiated area at week 2 ($p < 0.05$).

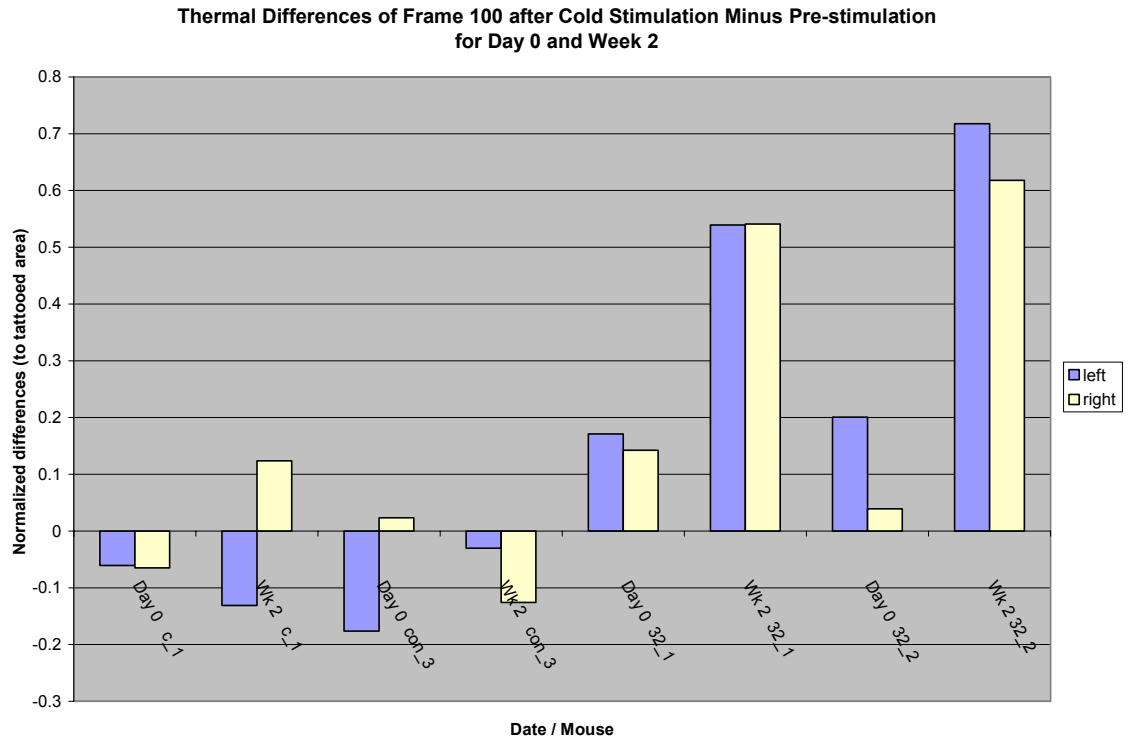


Figure 23. Typical result of reheating temperature differences of the left and right non-irradiated areas from radiated area of Frame 100 after the cold stimulation minus the initial temperature of the mouse on day 0 and week 2. Control mice are c_1 and con_3 and radiated mice are 32_1 and 32_2.

Significant differences from day 0 were not seen at day 1, week 1, or week 3 after radiation. To the left and right, and in the center of the tattooed area, the control mice reheated to the same temperature as their original temperatures. Therefore, the control mice did not show exhibit differences in reheating temperature differences from pre-stimulation ($p < 0.05$). Figure 24 shows plots of the thermal recovery of both a control and radiated mouse at the two week time point. The control mouse shows that all three areas return to ± 0.3 °C of their original temperatures after 8.25 minutes (Frame 100). The control mice and day 0 exhibited insignificant differences from the center ($p < 0.05$).

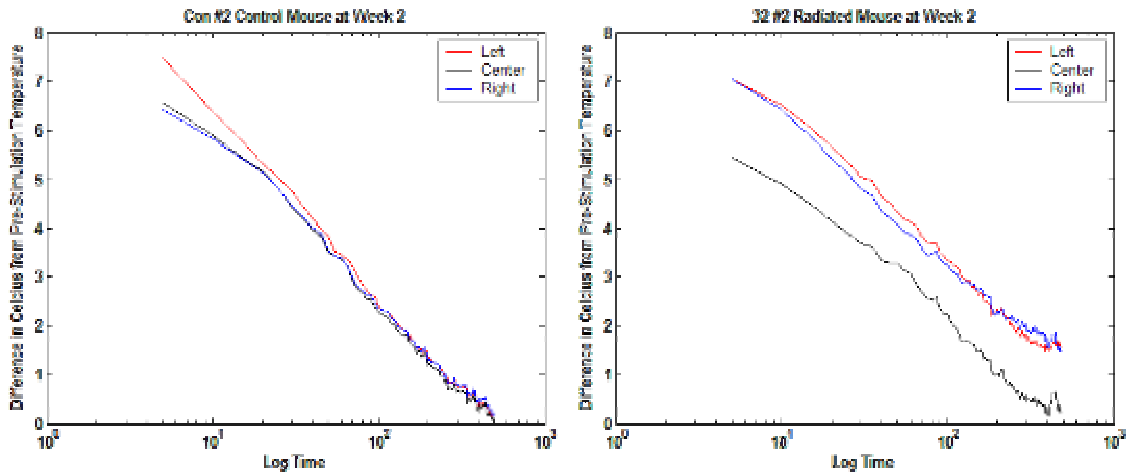


Figure 24. Differences in temperatures of irradiated (center) and non-irradiated (left and right) areas from the pre-stimulation temperature for (a) Control (#2) mouse at two weeks; and (b) 32 Gy (#2) mouse two weeks after radiation.

The 32 Gy (#2) mouse showed a faster reheating rate in the irradiated area than the left and right non-irradiated areas (Figure 24b) even though the irradiated area appeared much colder before the cold stimulation (Figure 26b). Figure 25 shows that the center returned to its original temperature, whereas the areas to the left and right of the tattooed area appear to be -2°C from their original temperatures.

Since the center was initially colder, the left and right non-irradiated areas should have returned to their original temperatures faster after the cold stimulation. Instead, all three areas increased 5°C after 100 frames. It was expected that the initially warmer areas before the stimulation would have increased in temperature more than the colder area.

Therefore, the change in thermal properties of the skin after irradiation was exhibited by a faster thermal recovery. The irradiated mice exhibited significant

temperature differences from day 0 between the non-irradiated areas and the irradiated area at week 2 ($p < 0.05$). The complete results of the temperature differences for the irradiated and control mice are shown in Appendix A.1.

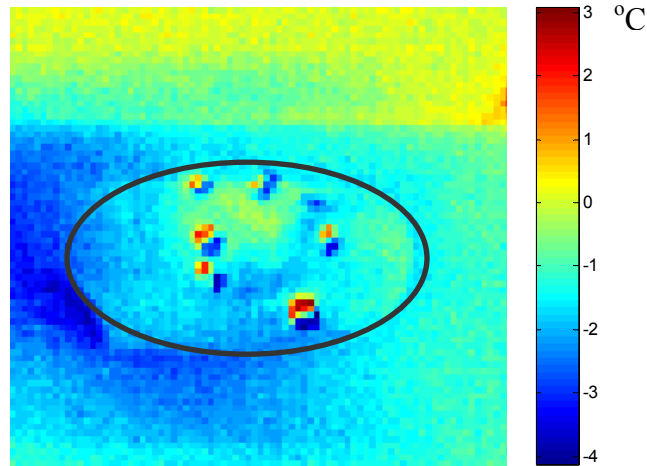


Figure 25. Difference in temperature of Frame 100 after the cold stimulation minus the pre-stimulation average temperature for the 32 Gy (#2) irradiated mouse two weeks after radiation.

5.1.2 Discussion of Changes in Thermal Recovery Times

The objective of this study in regards to thermography was to determine if there was a faster or slower thermal recovery after cold stimulation pre- and post-irradiation. Thermography was successful in detecting changes in the re-heating response; however, the technique only found significant results when the skin appeared inflamed, crusty, shedding and reddish, as seen in Figure 26a. These significant findings were essential, but it is important to remember that it was anticipated that this research would assess changes in the thermal properties of the skin before and after changes were visible by the naked eye. Thermal imaging detected a significant difference in the re-heating responses when the skin was visually inflamed ($p < 0.05$). Figure 26 shows a digital image and

static thermal image two weeks after radiation before the cold stimulation was performed. The radiated area was visibly and thermally recognizable on the mouse.

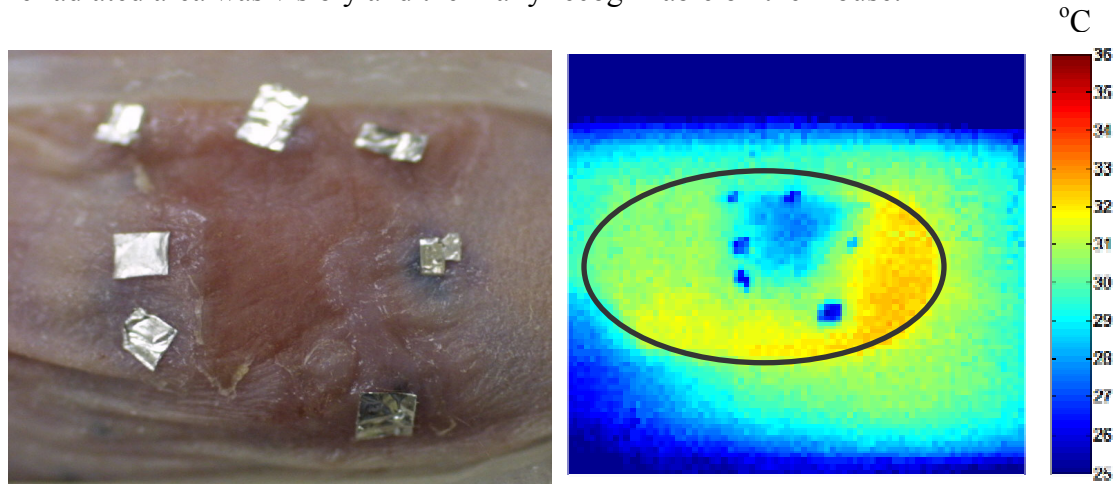


Figure 26. 32 Gy mouse (#2) two weeks after radiation in (a) Digital image with aluminum foil pieces covering the India ink tattoos. Red area inside tattoos is irradiated area showing desquamation; and (b) Static thermal image before cold stimulation showing affected areas to be colder in the image.

One challenge with comparing the temperature differences of the tattooed areas with the left and right non-tattooed areas was that the non-tattooed areas were not constant on day 1, week 1, and so on. Since there were no tattoos marking the non-irradiated areas, the area selected one day was not identical to the area selected the following week. Another source of variation in the experimental setup was that the ice cold water pack varied in temperature throughout each day and from one week to the next.

The thermography analysis met the objectives set forth in Chapter 3 by showing that the irradiated area re-heated significantly faster than the non-irradiated areas two weeks after radiation ($p < 0.05$). However, thermography did not detect significant changes in the re-heating rates before or after the acute changes of redness, inflammation, and shedding were visible.

5.2 Laser Doppler Imaging

5.2.1 Changes in Blood Flow

Laser Doppler imaging was selected as a technique to determine if a change in blood flow existed before and after the cold stimulation. The mean values for the LDI line scans did not show a significant change in blood flux before and after the cold stimulation ($p < 0.05$). A typical result of the blood flux before and after the cold stimulation is seen in Figure 27.

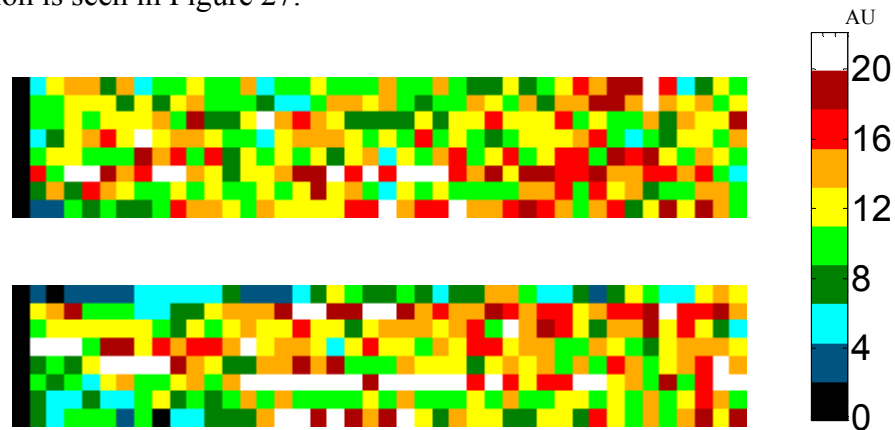


Figure 27. Blood flux of 32 Gy (#1) mouse (top) before cold stimulation and (bottom) after cold stimulation. The differences in blood flux were found to be not significant before and after the cold stimulation ($p < 0.05$) for all mice.

Although there is much variation in the microvasculature, the average value of the area was not significantly different before and after stimulation ($p < 0.05$). Figure 28 shows the quantitative blood flux values for six mice before any irradiation, recorded before and after the cold stimulation. With the knowledge that the blood flow did not significantly change after the cold stimulation, the changes in the skin thermal properties could be detected. Keeping the blood flow constant allowed only the skin properties to affect the thermal recovery time. Therefore, the thermal imaging results could be compared before

and after the cold stimulation and accepted. Complete results can be found in Appendix A.2.

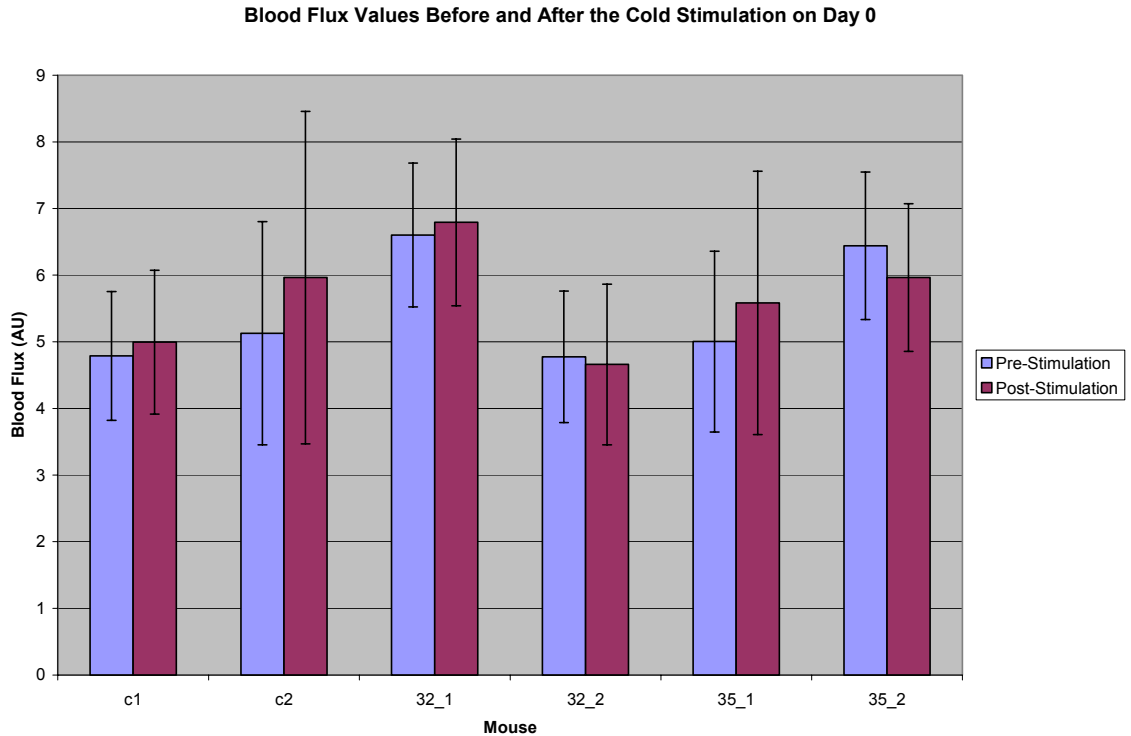


Figure 28. Laser Doppler blood flux values on day 0 before and immediately after the cold stimulation. No significant differences were found in the blood flow before and after the cold stimulation among all of the mice ($p < 0.05$).

5.3 Near-Infrared Multi-Spectral Imaging

5.3.1 Changes in Blood Oxygen Fraction

The objective in regards to the near-infrared multi-spectral imaging analysis was to non-invasively obtain diagnostically useful molecular information from embedded sites. From this, it could be determined if there were differences in oxygen blood saturation and blood volume before and after radiation and between the irradiated and non-irradiated mice.

All of the radiated mice showed relatively high blood oxygen saturation (mean = 86.5%) on day 0. However, after radiation, the normal tissue surrounding the radiated area continued to reconstruct as high oxygen saturation, but the irradiated area saturation decreased significantly in all of the radiated mice ($p < 0.05$). This significant decrease in blood oxygenation was seen at different time points after radiation, possibly depending on the radiation dose. The low reconstructed blood oxygen saturation values at the radiated site could be expected for a radiated area that was placing demands on the blood supply.

The change in the blood oxygenation for the 32 Gy (#2) mouse two weeks after radiation can be seen clearly in Figure 29. High levels of oxygen saturation seen inside the radiated area before radiation were no longer present two weeks after radiation.

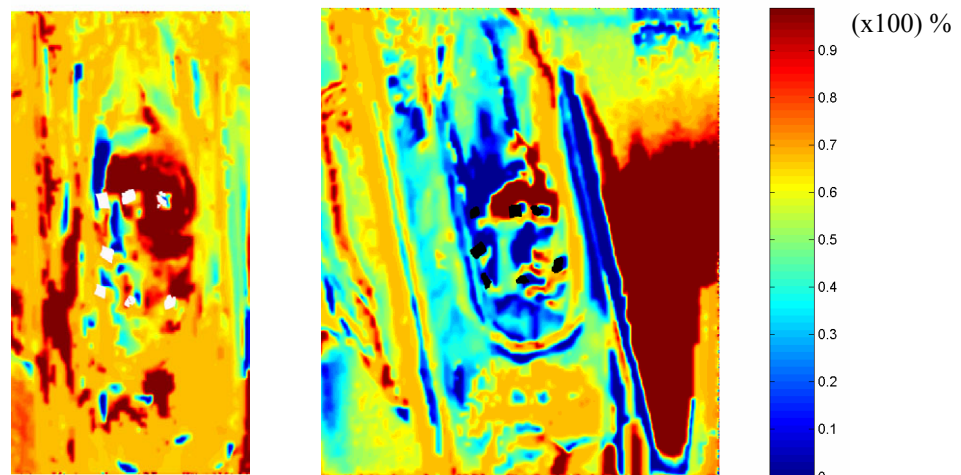


Figure 29. Oxygen blood saturation images of 32 Gy (#2) mouse (a) at day 0 before radiation; and (b) two weeks after radiation was applied. High oxygen saturation inside the radiated area before radiation was no longer present two weeks after radiation.

After a ROI was selected inside the tattooed area to determine the mean blood oxygen fraction before radiation and two weeks after radiation, a significant blood

oxygen saturation difference of over 60% ($p < 0.05$) was seen. Similar significant differences were seen for all mice ($p < 0.05$). The 32 Gy mouse (#1) showed a significant decrease in oxygen saturation one week after radiation ($p < 0.05$), still later than the higher dose mice of 35 Gy.

Another typical result is illustrated in Figure 30 of the 30 Gy radiated mouse (#1) at day 0 and two weeks after radiation when the significant decrease in blood oxygenation occurred ($p < 0.05$).

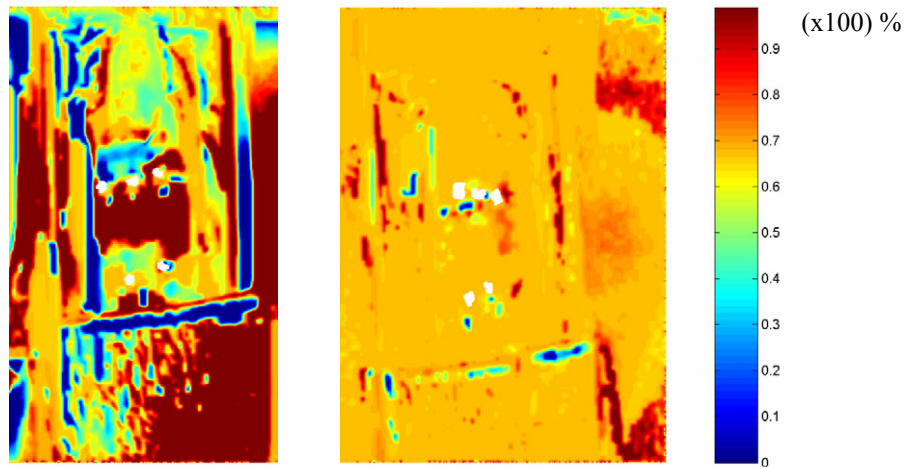


Figure 30. Oxygen blood saturation of 30 Gy (#1) mouse (a) at day 0 before radiation; and (b) two weeks after radiation was applied. High oxygen saturation inside the radiated area before radiation was no longer present two weeks after radiation.

Similar observations of significant decreases in blood oxygen fraction were seen in the remaining radiated mice, differing only in the time of onset of the significant decrease ($p < 0.05$). A table of the complete quantitative results can be found in Appendix A.3.

For the experimental analysis, Table 2 shows the date at which a significant decrease in blood oxygenation was observed, and the factor of change in blood

oxygenation levels for each radiated mouse.

Table 2. Date of significant decrease in blood oxygen fraction and the factor by which the fraction decreased for each radiated mouse.

Dose	Mouse	Date of Significant Blood Oxygen Fraction Decrease	Factor by which Blood Oxygen Fraction Decreased
35	2	Day 1	1.46
35	1	Week 1	1.26
32	1	Week 1	1.30
32	2	Week 2	3.53
30	1	Week 2	1.36
30	2	Week 4	1.40
30	3	Week 4	1.30

The mean blood oxygen fractions were determined by selecting a ROI inside the tattooed area identical to #2 in Figure 18. This mean blood oxygen fraction calculation of the radiated area was then compared on each day the experiment was conducted. The reconstructed values were not necessarily quantitatively correct, but the differences between the levels before radiation and at the time points listed in Table 2 proved to be significant ($p < 0.05$). The blood oxygenation generally decreased by a mean factor of 1.65. From Table 2, it appeared that the timing of the blood oxygen saturation decrease was dependent on the radiation dose. The higher the radiation dose, the faster the onset of the decrease in blood oxygen fraction, and vice versa. The blood oxygen fractions proved to be statistically significant ($p < 0.05$) when comparing blood oxygen fractions at day 0 with the blood oxygen fraction at the first time point that showed a decrease.

The blood oxygen fractions of the control mice on day 0 and week 1 (Figure 31) and the radiated mice on day 0 and the date in Table 2 (Figure 32) show quantitative differences.

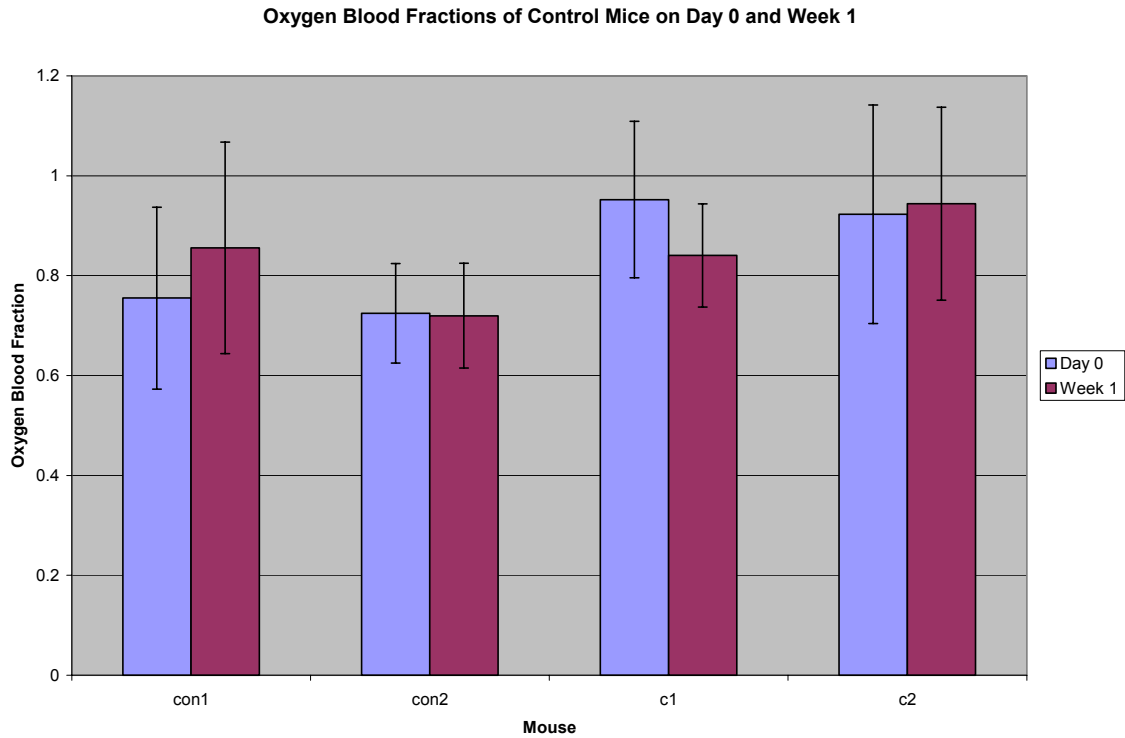


Figure 31. Blood oxygen fractions of control mice on day 0 and week 1. No significant differences were seen in blood oxygen fractions of the control mice ($p < 0.05$).

Week 1 differences from the original blood oxygen fractions among the control mice were found to be not significantly different ($p < 0.05$). Since the control mice underwent no radiation treatment, week 1 was randomly selected for comparison of the mice. Also, since the blood oxygen fractions of the control mice did not consistently decrease or increase from day 0 to week 1, there was no mean factor of change in the control mice.

On the other hand, the radiated mice showed significant oxygen blood fraction differences that ranged from one day to four weeks after the radiation (Figure 32). The blood oxygen fractions decreased by a mean factor of 1.65 when comparing day 0 to the time point when the initial significant decrease occurred. Compared to the control samples which had a maximum difference of approximately ± 0.1 throughout the

experiment, the changes seen in the radiated mice were significant ($p < 0.05$).

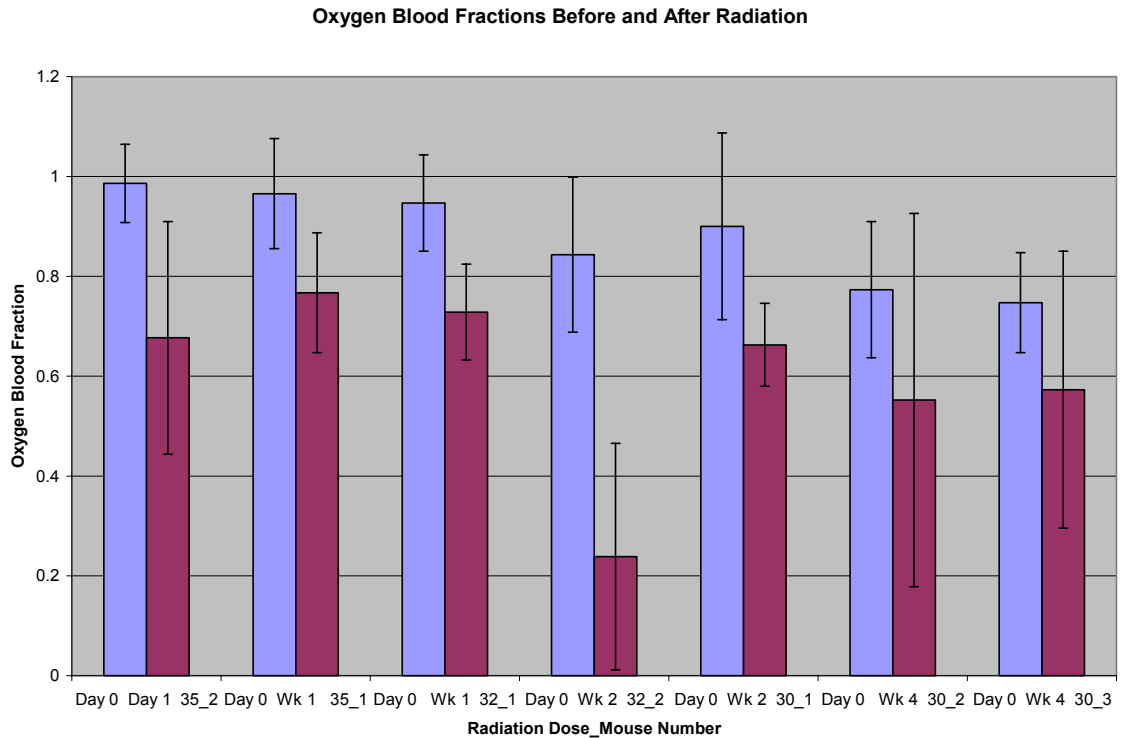


Figure 32. Blood oxygen fractions before and after radiation. Values after radiation were selected at the date of initial significant decrease in blood oxygen fraction from Table 2.

5.3.2 Changes in Blood Volume

The changes in blood volume were not as consistent as the changes in blood oxygen saturation. The general trend seen in four of the seven irradiated mice was a low initial blood volume (mean = 0.055) with an increase one week after radiation (mean = 0.26). Figure 33 shows the 32 Gy mouse (#1) reconstructed blood volume images at day 0 and week 1, which represents a typical example of increased blood volume seen in four out of seven of the irradiated mice.

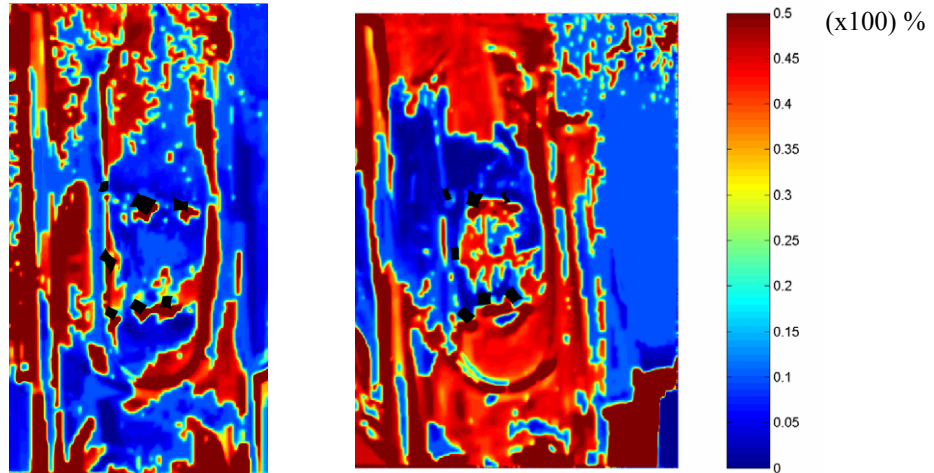


Figure 33. Blood volume fraction of 32 Gy (#1) mouse (a) before radiation at day 0; and (b) one week after radiation was applied. Inside the tattooed area, day 0 shows very small blood volume (mean = 0.09). One week after radiation, the tattooed area appears to have much higher blood volume (mean = 0.26).

The following figure shows the gradual increase of blood volume in the 35 Gy (#1) mouse over the first two weeks after radiation.

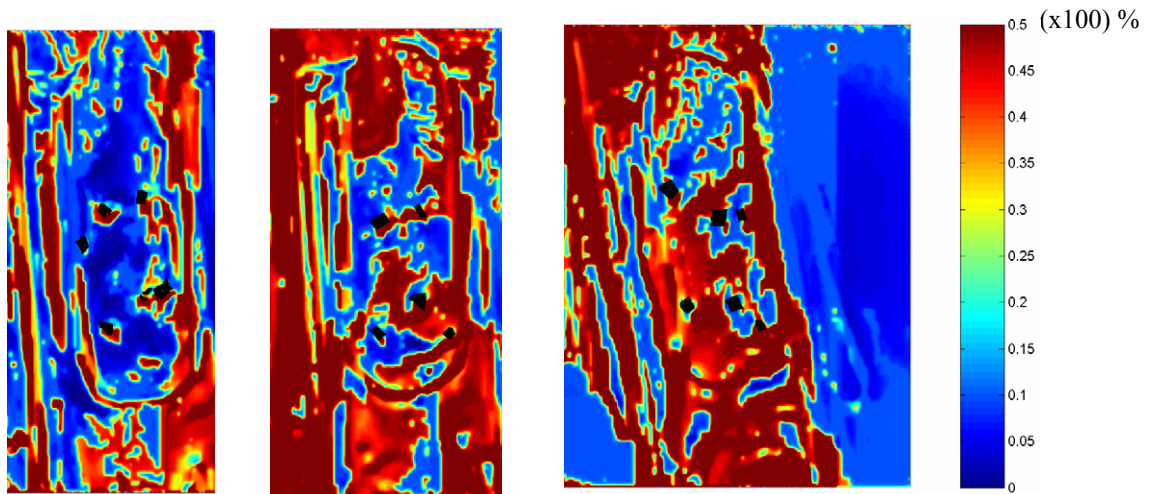


Figure 34. Blood volume fraction of 35 Gy (#1) mouse (a) before radiation at day 0; (b) one week after radiation was applied; and (c) two weeks after radiation was applied.

The mouse showed initial low blood volume (mean = 0.10). Then, one week after radiation, the blood volume increased inside the irradiated area (mean = 0.29), and after

two weeks, it increased even more (mean = 0.44).

Two other radiated mice started with a substantially high blood volume on day 0 (mean = 0.38) and presented lower values (mean = 0.10) one week after radiation. Figure 35 shows the 30 Gy (#3) irradiated mouse, which represents this phenomenon of a decrease in blood volume seen in two of seven irradiated mice. Since all seven irradiated mice did not behave consistently, it was difficult to substantiate the changes or provide any conclusions about blood volume. Complete results of blood volume changes can be seen in Appendix A.3.

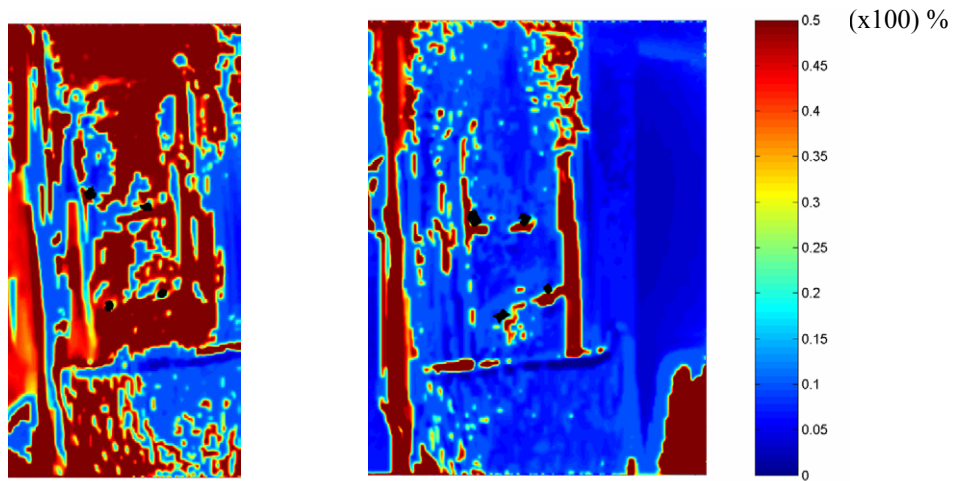


Figure 35. Blood volume fraction of 30 Gy (#3) mouse (a) before radiation at day 0; and (b) one week after radiation was applied.

5.3.3 Discussion of Changes in Blood Oxygen Fraction and Blood Volume

The multi-spectral imaging analysis was successful in finding significant differences before and after radiation in blood oxygen fractions for all of the radiated mice ($p < 0.05$) and changes in blood volume for a majority of the radiated mice.

Two major factors that affected the multi-spectral imaging analysis were movement and application of nail polish. The multi-spectral imaging analysis was

greatly affected by movement of the mice which caused large furrows and wrinkles. Figure 36 shows how extensive the wrinkle issue became for one mouse during the experiment.

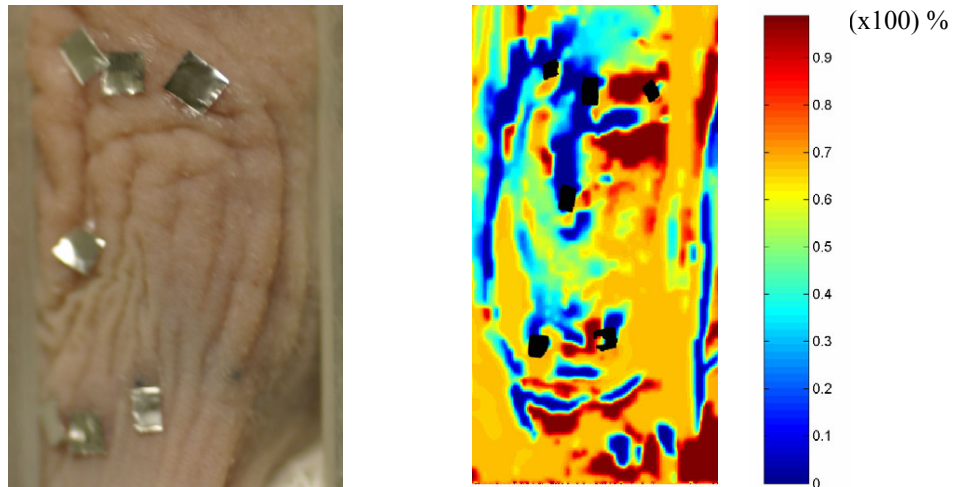


Figure 36. (a) Digital image of control mouse showing wrinkles; and (b) Reconstructed blood oxygen saturation of same control mouse showing non-homogeneity of saturation where wrinkles are present.

This caused incorrect values of blood flow and/or oxygenation to be reconstructed. The wrinkles could not be avoided in the reconstructed images, and thus had to be averaged as if the tissue was normal.

Another difficulty with the multi-spectral image reconstruction was the appearance of the nail polish. Nail polish adhered the aluminum foil pieces to the mouse skin. However, sometimes the nail polish spread to areas adjacent to the aluminum foil pieces as seen in Figure 37a. This caused changes in the reconstructed values of the blood oxygenation and volume.

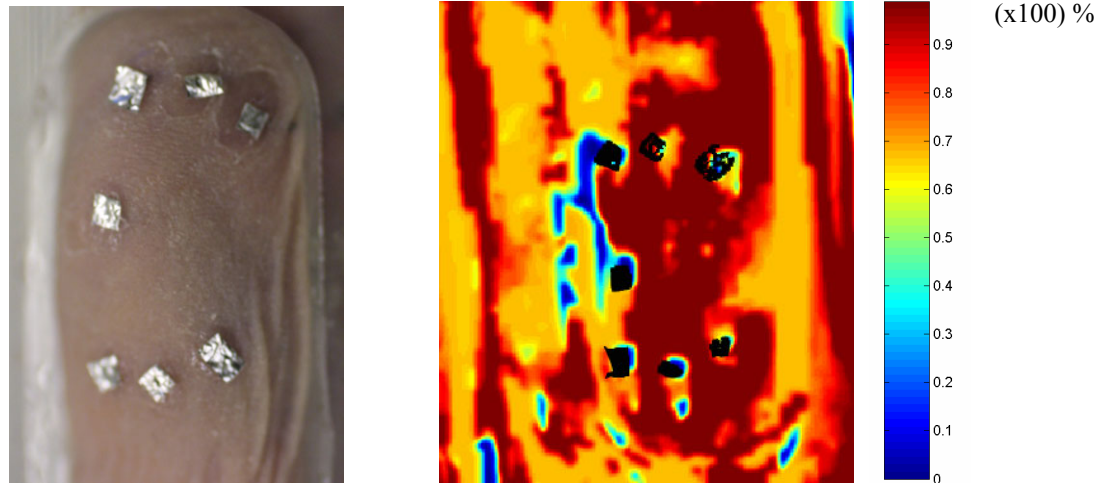


Figure 37. (a) Digital image of mouse showing spread of fingernail polish around aluminum foil pieces; and (b) Blood oxygen saturation showing fingernail polish areas. Areas with visible fingernail polish appeared to have lower blood oxygen saturation than the rest of the irradiated area.

Since mouse skin is very thin and the imaging devices see deeper than the skin tissue, some of the results could have been influenced by the organs underneath the skin. Figure 38 shows a particularly interesting pattern in the reconstructed blood oxygen saturation two weeks after radiation.

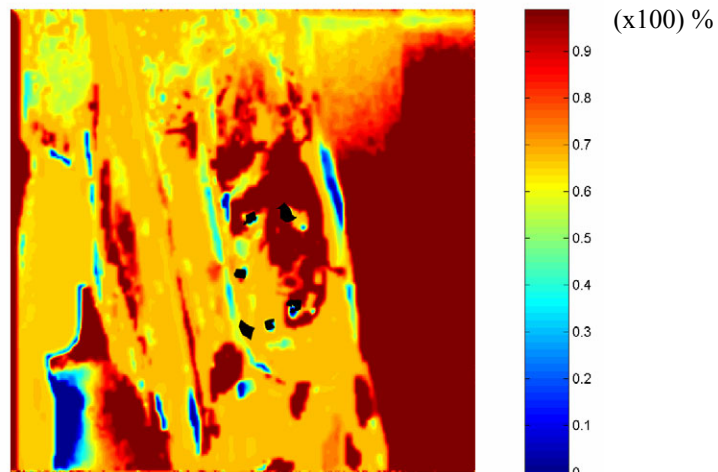


Figure 38. Blood oxygen fraction of the 32 Gy mouse (#1) two weeks after radiation showing bilateral pattern of oxygen re-saturation.

The radiated area shows a bilateral symmetry that may be indicative of some underlying process. Even with the aforementioned difficulties, the multi-spectral imaging analysis was successful in finding significant differences before and after radiation in blood oxygen fractions for all of the radiated mice ($p < 0.05$) and changes in blood volume for a majority of the radiated mice.

Chapter 6: Conclusions

Non-invasive imaging techniques were studied as methods of quantitatively analyzing the effects of radiation on mouse skin. The time-response thermography and near-infrared multi-spectral imaging analyses showed significant differences in the skin before and after the radiation ($p < 0.05$).

The thermography analysis found that the irradiated area reheated significantly faster than non-irradiated areas two weeks after radiation ($p < 0.05$). The analysis was successful when desquamation was present. However, when visible effects such as inflammation and shedding of the skin were not present, the thermography analysis did not conclude any significant changes.

The blood oxygen fraction was found to be significantly different before and after radiation ($p < 0.05$). The significant difference seemed to be dependent on the radiation dose level. The reconstructed blood volume images showed changes before and after radiation, but were not consistent. Four of seven irradiated mice showed low initial blood volumes that increased one week after radiation. Another two irradiated mice showed high initial blood volumes that decreased one week after radiation.

The experimental procedures and methods of analysis presented in this research show promise for the future of correlating dose with changes in the thermal skin properties, blood oxygen saturation, and blood volume.

Chapter 7: Suggestions for Further Study

The future of this experiment should be to use time-response thermography and near-infrared multi-spectral imaging to observe known areas of fibrosis and compare the results to non-fibrotic areas. Possible experimental subjects could include different strains of mice (nude vs. hairy), guinea pigs, and humans. These experiments should be performed first after the subject has fully developed chronic fibrosis (i.e. at least 12 weeks after radiation). Then it can be determined whether the proposed imaging techniques can quantitatively assess the differences in chronic fibrotic and non-fibrotic areas.

The first requirement for future experiments is the use of a temperature- and humidity-controlled room throughout the entire experiment. Additionally, future experiments should include tracking the weight of each subject. A smaller (lower weight) subject is generally believed to respond differently to radiation than a larger (greater weight) subject. In order to substantiate the claims of the blood oxygenation levels as well as the blood volume, these analytes need to be measured by a reliable technique before, during, and after the experimental testing. A larger sample size is also required in the future. Seven radiated (maximum of three for one radiation dose level) and five control mice were simply not enough to make appropriate conclusions.

Additionally, the cold stimulation should be based on temperature and not time. Each subject should be cooled down to the exact same temperature in order to see if the re-heating responses are identical or not. The cooling device for future experiments should be standardized as well. There were many difficulties in this experiment with the

ice cold water pack, including uneven cooling, different ice pack temperatures, and possible water condensation on the skin. Creating a new cooling technique would decrease the error in the thermography results. Further studies could also include using a 3-5 micron camera in addition to the 8-12 micron camera.

Some problems may arise when using the subjects mentioned above. If an area is imaged that contains hair, the images will have to be registered and the hairs will need to be removed before reconstruction of the data. Also, difficulties could arise in a human patient when finding a control non-irradiated area. Since fibrosis patients have cancerous tumors, it may be difficult to find an unaffected area. However, performing the procedures on a tattooed non-irradiated area would provide a large control area for the thermography and multi-spectral imaging analyses.

If changes can be found between the fibrotic and normal areas, future experiments should expand to begin before a subject undergoes radiation therapy. The experiments should be run at least twice a week. From the literature, it was learned that the first appearance of radiation damage (moist desquamation) would appear between 17-21 days after radiation. However, the images collected in this experiment were 14/15 and 21/25 days after radiation. Moist desquamation was seen in the images, but the peak of the reaction could have been missed since different radiation doses were applied and the metabolism of each mouse was different. Experiments run at least twice a week should detect more finite changes.

The future work of this study is to observe known areas of chronic fibrosis on different subjects to compare the results to non-fibrotic areas.

Appendix A

A.1 Thermal Recovery Results

Thermal recovery results of the left non-irradiated area are shown in Tables 3 and 4. The temperature difference of Frame 100 and the initial pre-stimulation temperature was calculated for the center irradiated and left and right non-irradiated areas. Then the left and right non-irradiated area differences were normalized to the center temperature difference.

Table 3. Temperature difference of the left non-irradiated area in °C from the center irradiated area.

Left Area*					
Gy Dose	#	Day 0 (°C)	Week 1 (°C)	Week 2 (°C)	Week 3 (°C)
30	1	-0.29	-0.41	0.43	-0.15
30	2	-0.19	0.11	0.37	0.01
30	3	-0.25	0.03	0.75	0.13
32	1	0.17	N/A	0.54	N/A
32	2	0.20	0.04	0.72	-0.09
35	1	N/A	0.01	0.35	N/A
35	2	0.18	-0.08	0.35	N/A
control	1	-0.06	-0.31	-0.13	N/A
control	2	-0.19	0.29	-0.18	N/A
control	3	N/A	N/A	-0.07	N/A
control	4	-0.40	-0.04	0.13	N/A
control	5	-0.18	-0.01	-0.03	N/A

* N/A denotes a value that could not be calculated because the area was too small to select a large region of interest.

Table 4. Temperature difference of the right non-irradiated area in °C from the center irradiated area.

Right Area*					
Gy Dose	#	Day 0 (°C)	Week 1 (°C)	Week 2 (°C)	Week 3 (°C)
30	1	-0.11	-0.05	0.49	-0.03
30	2	-0.20	-0.07	0.09	0.11
30	3	0.31	0.03	0.35	-0.44
32	1	0.14	-0.21	0.54	0.04
32	2	0.04	-0.13	0.62	-0.16
35	1	0.09	-0.01	0.46	N/A
35	2	0.02	0.02	0.20	N/A
Control	1	-0.06	0.19	0.12	N/A
Control	2	-0.31	-0.05	0.05	N/A
Control	3	-0.14	-0.32	-0.14	N/A
Control	4	-0.12	0.08	-0.16	N/A
Control	5	0.02	0.06	-0.13	N/A

* N/A denotes a value that could not be calculated because the area was too small to select a large region of interest.

A.2 Laser Doppler Imaging Results

Table 5. Laser Doppler imaging blood flux of mice on day 0.

Gy Dose	#	Before Cold Stimulation (AU)	Std Deviation	After Cold Stimulation (AU)	Std Deviation	Difference in Blood Flux (AU)
Control	1	4.79	0.96	4.99	1.08	-0.21
Control	2	5.13	1.67	5.96	2.49	-0.84
32	1	6.60	1.08	6.79	1.25	-0.19
32	2	4.77	0.99	4.66	1.21	0.11
35	1	5.00	1.36	5.58	1.98	-0.58
35	2	6.44	1.11	5.96	1.11	0.48

A.3 Near-Infrared Multi-Spectral Imaging Results

Table 6. Oxygen blood fraction analysis of radiated and control mice.

Gy Dose	#	Date	# Pixels	Mean Oxygen Blood Fraction (x100)%	Std. Dev.	Oxygen Blood Fraction Difference from Day 0
32	2	Day 0	3411	0.84	0.16	0.00
		Day 1	3030	0.93	0.12	0.09
		Week 1	2593	0.98	0.08	0.13
		Week 2	1871	0.24	0.23	-0.60
		Week 3	1990	0.64	0.33	-0.20
32	1	Day 0	4262	0.95	0.10	0.00
		Day 1	3975	0.99	0.06	0.05
		Week 1	3765	0.73	0.10	-0.22
		Week 2	3669	0.87	0.14	-0.08
		Week 3	3370	0.70	0.27	-0.25
35	1	Day 0	3132	0.97	0.11	0.00
		Day 1	3546	0.80	0.35	-0.16
		Week 1	2783	0.77	0.12	-0.20
		Week 2	2900	0.71	0.09	-0.26
		Week 3	3229	0.80	0.25	-0.17
35	2	Day 0	4496	0.99	0.08	0.00
		Day 1	4102	0.68	0.23	-0.31
		Week 1	4058	0.96	0.08	-0.03
		Week 2	3576	0.99	0.07	0.00
		Week 3	4395	0.90	0.26	-0.09
30	1	Day 0	5652	0.90	0.19	0.00
		Day 1	5850	0.77	0.20	-0.13
		Week 1	6191	0.68	0.04	-0.22
		Week 2	6202	0.66	0.08	-0.24
		Week 3	4911	0.77	0.26	-0.13

Gy Dose	#	Date	# Pixels	Mean Oxygen Blood Fraction (x100)%	Std. Dev.	Oxygen Blood Fraction Difference from Day 0
30	2	Day 0	5168	0.77	0.14	0.00
		Day 1	2768	0.65	0.11	-0.12
		Week 1	5639	0.88	0.13	0.11
		Week 2	3592	0.88	0.13	0.10
		Week 3	4509	0.84	0.13	0.07
		Week 4	3897	0.55	0.37	-0.22
30	3	Day 0	6317	0.75	0.10	0.00
		Day 1	5023	0.79	0.15	0.05
		Week 1	4495	1.00	0.02	0.25
		Week 2	4140	0.86	0.19	0.11
		Week 3	3771	0.80	0.14	0.05
		Week 4	3485	0.57	0.28	-0.17
Control	1	Day 0	4463	0.76	0.18	0.00
		Day 1	5229	0.65	0.05	-0.10
		Week 1	5573	0.86	0.21	0.10
		Week 2	6774	0.88	0.16	0.13
		Week 3	5501	0.82	0.18	0.07
Control	2	Day 0	3854	0.72	0.10	0.00
		Day 1	8450	0.68	0.11	-0.04
		Week 1	3803	0.72	0.11	0.00
		Week 2	7922	0.59	0.23	-0.14
		Week 3	2198	0.58	0.39	-0.15
Control	3	Day 0	4063	0.95	0.16	0.00
		Day 1	3551	0.95	0.10	0.00
		Week 1	1817	0.84	0.10	-0.11
		Week 2	3670	0.95	0.08	0.00
		Week 3	3111	0.27	0.29	-0.69
Control	4	Day 0	3580	0.92	0.22	0.00
		Day 1	4080	0.98	0.07	0.06
		Week 1	3132	0.94	0.19	0.02
		Week 2	2979	0.98	0.05	0.06
		Week 3	2561	0.74	0.38	-0.18

Table 7. Blood volume analysis of radiated and control mice.

Gy Dose	#	Date	# Pixels	Mean Blood Volume (x100) %	Std. Dev.
32	2	Day 0	3411	0.02	0.01
		Day 1	3030	0.01	0.03
		Week 1	2593	0.06	0.05
		Week 2	1871	0.01	0.01
		Week 3	1990	0.03	0.01
32	1	Day 0	3897	0.10	0.07
		Week 1	3765	0.27	0.14
		Week 2	3669	0.10	0.12
		Week 3	3370	0.09	0.08
35	1	Day 0	4551	0.10	0.11
		Day 1	3546	0.01	0.01
		Week 1	4172	0.29	0.18
		Week 2	2900	0.44	0.11
		Week 3	3229	0.04	0.03
35	2	Day 0	4496	0.01	0.01
		Day 1	4102	0.02	0.02
		Week 1	4058	0.14	0.09
		Week 2	3576	0.01	0.02
		Week 3	4395	0.04	0.04
30	1	Day 0	5652	0.01	0.03
		Week 1	6191	0.36	0.16
		Week 2	6202	0.06	0.04
		Week 3	4911	0.03	0.04
30	2	Day 0	6331	0.38	0.18
		Day 1	2768	0.21	0.18
		Week 1	5639	0.13	0.14
		Week 2	3592	0.03	0.02
		Week 3	4509	0.25	0.17
30	3	Day 0	6317	0.38	0.16
		Day 1	5023	0.28	0.18
		Week 1	4495	0.07	0.01
		Week 2	4140	0.02	0.02
		Week 3	3771	0.44	0.15
Control	2	Day 0	3580	0.02	0.03
		Week 2	2979	0.02	0.02
		Week 3	3961	0.00	0.00

Bibliography

- Al-Barwari, S., and C. Potten (1976). "Regeneration and dose-response characteristics of irradiated mouse dorsal epidermal cells." *Int. J. Radiat. Biol.* **30**(3): 201-216.
- Archambeau, J. O., A. Ines and L.F. Fajardo (1985). "Correlation of the Dermal Microvasculature Morphology with the Epidermal and the Endothelial Population Changes Produced by Single X Ray Fractions of 1649, 2231 and 2619 rad in Swine." *Int. J. Radiat. Oncology Biol. Phys.* **11**: 1639-1646.
- Archambeau, J. O., R. Pezner and T. Wasserman (1995). "Pathophysiology of Irradiated Skin and Breast." *Int. J. Radiat. Oncology Biol. Phys.* **31**(5): 1171-1185.
- Autio, P., T. Saarto, M. Tenhunen, I. Elomaa, J. Risteli and T. Lahtinen (1998). "Demonstration of increased collagen synthesis in irradiated human skin in vivo." *British Journal of Cancer* **77**(12): 2331-2335.
- Bourgeois, J. F., S. Gourgou, A. Kramar, J.M. Lagarde, Y. Gall and B. Guillot (2003). "Radiation-induced skin fibrosis after treatment of breast cancer: profilometric analysis." *Skin Research and Technology* **9**: 39-42.
- Burger, A., H. Loffler, M. Bamberg and H.P. Rodemann (1998). "Molecular and cellular basis of radiation fibrosis." *Int. J. Radiat. Biol.* **73**(4): 401-408.
- Canada (2002). Radiation - Quantities and Units of Ionizing Radiation, Canadian Centre for Occupational Health and Safety. [Online]. Available WWW: http://www.ccohs.ca/oshanswers/phys_agents/ionizing.html.
- De Ruiter, J., and L.M. Van Putten (1975). "Measurement of Blood Flow in the Mouse Tail After Radiation." *Radiation Research* **61**: 327-438.
- Delanian, S., F. Baillet, J. Huart, J.-L. Lefaix, C. Maulard, M. Housset (1994). "Successful treatment of radiation-induced fibrosis using liposomal Cu/Zn superoxide dismutase: clinical trial." *Radiotherapy and Oncology* **32**: 12-20.
- FDA (2003). Whole Body Scanning Using Computed Tomography (CT). [Online]. Available WWW: <http://www.fda.gov/cdrh/ct/rqu.html>.
- Field, S. B., R.L. Morgan and R. Morrison (1976). "The Response of Human Skin to Irradiation with X-rays or Fast Neutrons." *Int. J. Radiat. Oncology Biol. Phys.* **1**: 481-486.

- FLIR (2002). Thermography, FLIR Infrared Camera Systems, Inc. [Online]. Available WWW: <http://www.flirthermography.com>.
- Gandjbakhche, A. H., and G.H. Weiss (1995). "Random walk and diffusion-like models of photon migration in turbid media." *Progress in Optics* **34**(5): 335-402.
- Gottlober, P., G. Bezold, L. Weber, P. Gourmelon, J.M. Cosset, W. Bahren, H.J. Hald, T.M. Fliedner and R.U. Peter (2000). "The radiation accident in Georgia: Clinical appearance and diagnosis of cutaneous radiation syndrome." *J. Am. Acad. Dermatol.* **42**(3): 453-458.
- Griffiths, A., J. Miller, D. Suzuki, R. Lewontin, and W. Gelbart (2000). An Introduction to Genetic Analysis. New York, WH Freeman and Co.
- Hattery, D., M. Hassan, S. Demos, and A. Gandjbakhche (2002). "Hyperspectral Imaging of Kaposi's Sarcoma for Disease Assessment and Treatment Monitoring." *31st Applied Imagery Pattern Recognition Workshop*.
- Head, J. F., and R. L. Elliott (2002). "Infrared imaging: Making progress in fulfilling its medical promise." *IEEE Eng. Med. Biol. Mag.* **21**(6): 80-85.
- Hirota, S., K. Tsujino, T. Oshitani, Y. Hishikawa, Y. Takada, M. Kono and M. Abe (2002). "Subcutaneous Fibrosis After Whole Neck Irradiation." *Int. J. Radiat. Oncology Biol. Phys.* **52**(4): 937-943.
- Hoeller, U., A. Kuhlmeier, A. Bajrovic, K. Grader, J. Berger, S. Tribius, F. Fehlauer and W. Alberti (2003). "Cosmesis from the patient's and the doctor's view." *Int. J. Radiat. Oncology Biol. Phys.* **57**(2): 345-354.
- Hopewell, J. W. (1990). "The skin: its structure and response to ionizing radiation." *Int. J. Radiat. Biol.* **57**(4): 751-773.
- Illsley, M., J.H. Peacock, R.J. McNulty and J.R. Yarnold (2000). "Increased collagen production in fibroblasts cultured from irradiated skin and effect of TGF B1 - clinical study." *British Journal of Cancer* **83**(5): 650-654.
- Iwakawa, M., S. Noda, T. Ohta, C. Ohira, R. Lee, M. Goto, M. Wakabayashi, Y. Matsui, Y. Harada and T. Imai (2003). "Different Radiation Susceptibility among Five Strains of Mice Detected by a Skin Reaction." *J. Radiat. Res.* **44**: 7-13.
- Johansen, J., F. Taagehoj, T. Christensen, J. Overgaard and M. Overgaard (1994). "Quantitative magnetic resonance for assessment of radiation fibrosis after post-mastectomy radiotherapy." *The British Journal of Radiology* **67**: 1238-1242.

- Kelch, C., and R.J. Seffrin (1998). Infrared Thermography for PPM. Maintenance Technology, Applied Technology Publications, Inc. **2002**. [Online]. Available WWW: <http://www.mt-online.com/current/05-99amt01.html>
- Lahtinen, T., J. Nuutinen, E. Alanen, M. Turunen, L. Nuortio, T. Usenius and J. Hopewell (1999). "Quantitative Assessment of Protein Content in Irradiated Human Skin." *Int. J. Radiat. Oncology Biol. Phys.* **43**(3): 635-638.
- Lefaix, J. L., S. Delanian, M.C. Vozenin, J.J. Leplat, Y. Tricaud and M. Martin (1999). "Striking Regression of Subcutaneous Fibrosis Induced by High Doses of Gamma Rays Using a Combination of Pentoxifylline and a-Tocopherol: an Experimental Study." *Int. J. Radiat. Oncology Biol. Phys.* **43**(4): 839-847.
- Lopez, A., A. Bazerbashi, C. Stefanato and T. Phillips (1998). "What is your Diagnosis?" *Wounds* **10**(4): 132-135.
- Love, T. J. (1980). "Thermography as an indicator of blood perfusion." *Ann. N.Y. Acad. Sci.* **335**: 429-437.
- Maxwell-Cade, C. (1968). "Principles and practices of clinical thermography." *Radiography* **34**(398): 23-34.
- Merla, A., L. Di Donato, S. Di Luzio, and G.L. Romani (2002). "Quantifying the Relevance and Stage of Disease with the Tau Image Technique: A Complimentary Diagnostic Imaging Technique Based on Infrared Functional Imaging." *IEEE Engineering in Medicine and Biology* **21**(6): 86-91.
- Moor-LDI (2002). Laser Doppler Imager, Moor Instruments, Inc. [Online]. Available WWW: <http://www.moor.co.uk>.
- Napier, I. (1999). "Reference dose for dental radiography." *British Dental Journal* **186**(8): 392-396.
- NIH (2002). Radiotherapy, National Cancer Institute. [Online]. Available WWW: <http://www.cancer.gov>.
- NIH (2003). Radiation Therapy and You: A Guide to Self-Help During Cancer Treatment, National Cancer Institute. [Online]. Available WWW: <http://www.cancer.gov>.
- NRPB (2000). Referral guidelines for imaging. Radiation Protection. Italy, European Commission. [Online]. Available WWW: <http://europa.eu.int/comm/environment/radprot/118/rp-118-en.pdf>.

- Remy, J., J. Wegrowski, F. Crechet, M. Martin and F. Daburon (1991). "Long-Term Overproduction of Collagen in Radiation-Induced Fibrosis." *Radiation Research* **125**: 14-19.
- Riekki, R., A. Jukolla, M-L. Sassi, M. Hoyhtya, M. Kallioinen, J. Risteli and A. Oikarinen (2000). "Modulation of skin collagen metabolism by irradiation: collagen synthesis is increased in irradiated human skin." *British Journal of Dermatology* **142**: 874-880.
- Roper (2003). NTE/CCD Detector User Manual, Trenton, Princeton Instruments.
- Russo, A. (2002). Normal Tissue Protection against Ionizing Radiation. Animal Study Proposal. Bethesda, Maryland, National Cancer Institute, National Institutes of Health.
- Sarikaya, M., and I. Aksay (1995). Biomimetics: Design and Processing of Materials. New York, American Institute of Physics Press.
- USA (2002). Ionizing Radiation Safety, Understanding Radiation, Environmental Protection Agency. [Online]. Available WWW: <http://www.epa.gov>.
- Usuki, K., T. Kanekura, K. Aradono, and T. Kanzaki (1998). "Effect of nicotine on peripheral cutaneous blood flow and skin temperature." *J. Derm. Sci.* **16**: 173-181.